Chapter One

1.0 Introduction

The question of chain organization within the ordered structure of heterogeneous block copolymers in bulk has been addressed extensively in the past for wholly amorphous and semicrystalline block copolymers. In semicrystalline block copolymers, it has been presumed that random coils exist in the amorphous domains and that conventional chain folding (i.e. chains parallel to or perhaps slightly inclined with respect to the normals) takes place in the crystalline domains. In homogeneous melt or solution crystallization where crystallization precedes microphase separation, much information on the behaviour is known and conventional chain folding occurs. In this case, when crystallization occurs, it must take place within a confined already-ordered, heterogeneous morphology[1].

Kofina and Cohen[2] investigated the lattice unit orientation with respect to the lamellar microstructure for a semicrystalline diblock copolymers containing a crystallizable ethylene block. The orientation of the crystallized ethylene chains was found to be perpendicular to the lamellar normals. This unusual chain alighnment was attributed to the influence of interface-dominated nucleation and topological constraints on growth when the ethylene block chain crystallize within the amorphous lamellar microdomains. Bates and co-workers[3-5] have studied the lamellar orientation of nearly symmetric amorphous poly(ethylethylene)/poly(ethylene-propylene) (EE/EP) diblock copolymer samples, which were textured using large strain dynamic shear. Near the order-disorder transition (ODT) temperature, and at low shear frequencies, the lamellae arrange parallel to the plane of shear, while higher frequency processing leads to lamellae perpendicular to the plane of shear. At temperatures further below the ODT the parallel lamellae orientation is obtained at all shearing frequencies. These interesting and unexpected results prompted me to inquire into the possibility of lamellar orientation morphology of my sample under shear.

Block copolymers are macromolecules composed of blocks of chemically distinct repeat units. Because of the incompatibility, block copolymers usually microphase-separate into well-ordered nanoscale structures below an order-disorder transition temperature. Depending on the volume fraction of components, lamellae, gyroids, cylinders, and spheres have been observed[6]. Based on the degree of incompatibility χN, where χ is the Flory-Huggins segmental interaction parameter and N is the total degree of polymerization, two typical limiting regimes have been identified: the weak segregation limit (WSL) with χN close to $(\chi N)_{ODT}$ (ODT is the order-disorder transition temperature) (for symmetric diblocks, $(\chi N)_{ODT} = 10.5$ in the mean field limit) and the strong segregation limit (SSL) with $\chi N \gg 10.5$. In the WSL regime, the composition profile is essentially sinusoidal, whereas in the asymptotic SSL limit the components are essentially pure and the interphase between them is narrow. In the case of diblock copolymers, if one of the blocks is crystallizable or liquid-crystalline and the other block is amorphous, the inherent complexity of such block copolymers will be greatly increased.

The final phase structure and crystalline morphology in amorphous-crystalline block copolymers depend on the competition between three phase transitions, that is, the order-disorder transition of the diblock copolymer, the crystallization of the crystallizable block, and the vitrification of the amorphous block. Depending on the order-disorder transition temperature T_{ODT}, the melting temperature T_m, and the glass transition temperature of the amorphous block T_g, both unconfined and confined crystallization have been observed[6]. For unconfined crystallization, the phase separation between the blocks is driven by crystallization of the crystallizable block, or the crystallization interaction overwhelms the microphase separation, resulting in alternating crystalline and amorphous lamellae. For crystallization confined within the ordered phase morphology, depending on the volume fraction, the confinement geometries include lamellae, cylinders, and spheres. If crystallization and the order-disorder transition start at the same time with small and comparable rates, the dynamic coupling and kinetic competition between crystallization and microphase separation can result in a more complex morphology.

In our block copolymer system, the mophology of the Polystyrene-PolyOctadecylmethacrylate (PS-PODMA) block copolymer with the PODMA composition $f_{PODMA} = 0.39$ was determined to have lamellar morphology after microphase-separation while the $f_{PODMA} = 0.18$ reveal a cylindrical structure. The onset of melting of the former and the latter systems are around 28 and 11^0C respectively while the onset of crystallization are around 22 and 11^0C. The degree of crystallinity for the lamellar structure is 25 mol% and its 15 mol% for the cylindrical structure. In all two samples, the PolyOctadecylmethacrylate domain is in the confined geometry of the amorphous polystyrene. There is a side chain crystallization of the side chain methylene unit.

The crystallographic and morphological analysis were examined using Wide- and Small-angle X-ray scattering and two dimensional small and wide angle scattering. The lattice unit cell orientation as well as lamellar superstructure orientation were determined. Raman spectroscopy was also employed to investigate the stretching vibrations in the molten state.

.

Chapter Two -Block copolymers

2.0   Overview

Block copolymers consist of two or more polymer sequence in the main chains that are combined with each other. For example, the A-b diblock copolymer composed of two kinds of polymer component A and B, has order and structure at thermal equilibrium after becoming solid from polymer solution or molten state. Those structures are determined by the balance between the entropy that enforces polymer miscibility and the enthalpy that makes polymers' phase separate from each other. In other words, when the segregation strength between A and B is dominant, unit-A and unit-B segregates and microphase- separated structure consisting of phase A and phase B is formed[7].

The architecture of this block copolymers can be controlled by the synthesis procedure, and it is possible to prepare diblock, triblock, multiblock, starblock and graft copolymers. These are illustrated in the figure below[8]. The possibilities of molecular design seem to be almost limited, only being limited by the chemist's imagination.
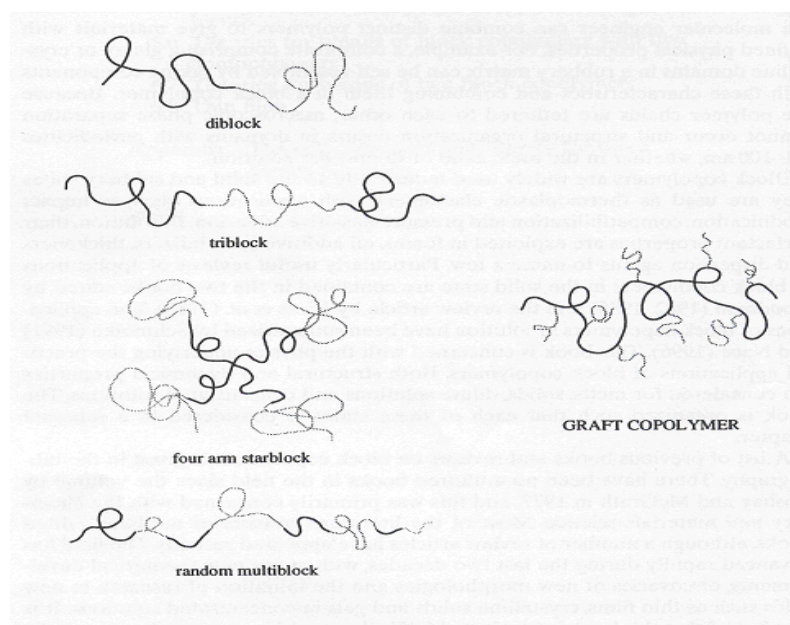

Figure. 2.1 : Types of Block Copolymers

2.1 Structures of Block copolymers

Two competing effects govern the thermodynamics of the block copolymer melts. At high temperatures, the chains are mixed homogeneously, as in any polymer melt. As the temperature is reduced, the tendency for the blocks to segregate is enhanced, i.e. the enthalpy driven process of demixing is favoured. However, this is necessarily accompanied by a reduction in entropy as the chain configuration becomes more constrained. The extent of segregation of the copolymer may then be

expressed using the reduced parameter χN. Where χ is the Flory-Huggins interaction parameter, which contains a significant enthalpic contribution and is governed by the incompatibility of monomers[9] , and N is the copolymer degree of polymerization, reflecting the N-dependent translational and configurational entropy.

$$\Delta F^m = RT\left[\frac{\phi_1}{N_1}\ln\phi_1 + \frac{\phi_2}{N_2}\ln\phi_2 + \chi\phi_1\phi_2\right] \; ; \; \phi_1 + \phi_2 = 1$$

Where ϕ_1, ϕ_2 and N_1, N_2 are the volume fractions and degree of polymerization of the two polymers.

$$\chi < 0 \quad \rightarrow \text{Miscibility (of the two polymers)}$$

$$\chi < \chi_{cr} \quad \text{and} \quad \chi_{cr} = \frac{1}{2}\left(\frac{1}{\sqrt{N_1}} + \frac{1}{\sqrt{N_2}}\right)^2$$

The tendency of the blocks to segregate on lowering the temperature leads to a process termed microphase separation, where separation of the components occurs into nanoscale domains. Microphase separation is indicated in the figure below.
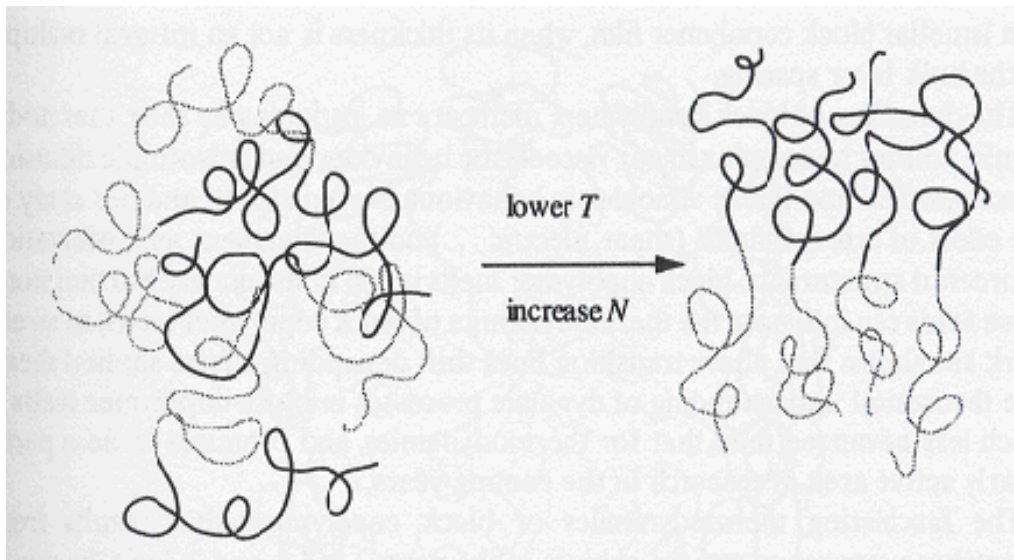

Figure: 2.2 Microphase Separation in block Copolymer melt

Phase separation on the macroscopic level is prevented by the connectivity of the polymer chains that defines block copolymers. The transition from a homogeneous melt of chains to a heterogeneous melt of ordered microphase-separated domains is called the order-disorder transition (ODT)[8]. It occurs at a critical value of χN, depending on the composition of the copolymer, which is parameterized by f. For a symmetric ($f = 0.5$) diblock, with equal segment sizes, mean field theory predicts a critical $(\chi N)_{ODT} = 10.5$, compared to $(\chi N) = 2.0$ for a phase separation in a symmetric polymer blend. The

ordered phase that is formed for $\chi N > (\chi N)_{ODT}$ depends on the composition of the copolymer, which determines the curvature of the interface between blocks and their packing density.

The melt phase behaviour is thus summarized in the phase diagrams parameterized by f and χN. Three regimes have been defined depending on the extent of segregation of the blocks:

Weak   regime   :($\chi N \approx 10$)

Intermediate regime   :($\chi N \approx 10\text{-}100$)

Strong regime   :($\chi N \approx 10 > 100$) i.e. approximately greater that 100.

In the weak regime limit, the composition profile is approximately sinusoidal, i.e. the volume fraction of one of the blocks varies sinusoidally about the average value. As χN increases, the profile becomes sharper, with a narrower interphase between blocks and saturation of the composition so that in the strong segregation limit the domains contain essentially pure components. The phase behaviour in the strong segregation limit depends largely on the composition of the copolymer f[8]. However, for weakly segregated copolymers, in addition to f and χN, the degree of polymerization, N, is an independent variable relevant to the phase behaviour. It controls the composition fluctuations which are important for block copolymers near the order-disorder transition. There are known equilibrium mesophases for diblock copolymers (spheres, cylinders, gyroid, and lamellae) shown in the phase diagram below are.
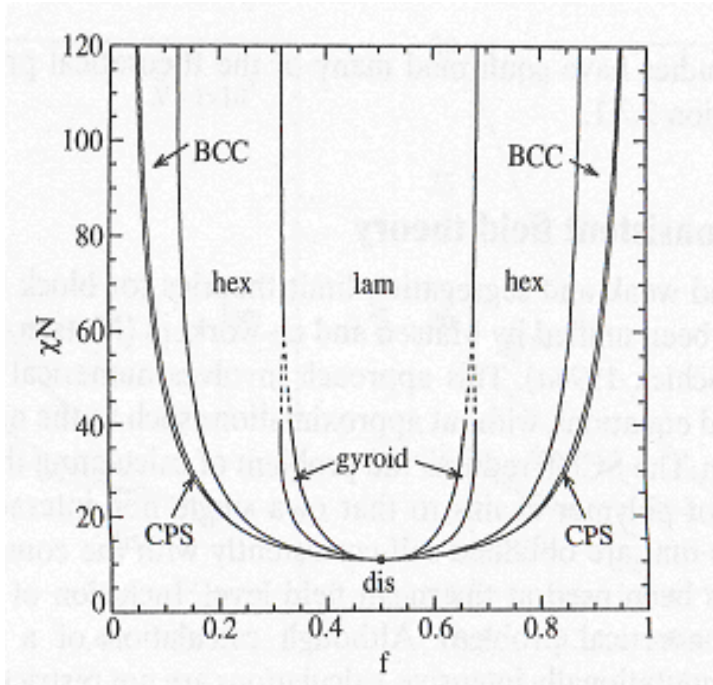

Figure 2.3 : Phase diagram for a conformationally-symmetric diblock copolymer

Furthermore, in the melt, block copolymers can self-assemble into a variety of ordered structures via the process of microphase separation. Microphase separation is driven by the enthalpy of demixing of the constituent components of the block copolymers, whilst macrophase separation is prevented by the

chemical connectivity of the blocks. This enthalpy is proportional to the Flory-Huggins segmental interaction parameter χ, which is found to be inversely proportional to temperature and is usually parameterized as $\chi = A/T + B$ as shown above. Microphase separation leads to ordered structures with periods of several R_g, where R_g is the copolymer radius of gyration[8]. The entropic penalty associated with the chain stretching is proportional to the degree of polymerization N. As already said, the product χN that expresses the enthalpic-entropic balance is then used to parameterize the block copolymer phase behaviour, along with the composition.

2.2 Crystallization of Semicrystalline block copolymers

Semicrystalline block copolymers usually show richness in morphology due to the competition between microphase separation and crystallization. Crystallization behavior of rubber/crystalline block copolymers is determined by segregation strength as well as morphology. Strong segregation strength can lead to confined crystallization and thus the morphology in the melt is preserved after crystallization, whereas weak segregation strength may result in breakout crystallization and lamellar structure is formed in the solid irrespectively of the morphology in the melt[10]. Confined and breakout crystallization also show different kinetic characteristics: homogeneous nucleation at very low crystallization temperature, nucleation-controlled crystallization rate, Avrami exponent $n = 1.0$ and strong dependence on T_c of crystallization half-time for confined crystallization, while Avrami exponent from 2.0 to 4.0 with heterogeneous nucleation and weak dependence on T_c of crystallization half-time for breakout crystallization.

Crystallization behaviour of glassy/crystalline block copolymers strongly depends on crystallization temperature and order–disorder transition temperature (T_{ODT}) of the block copolymers. Confined crystallization occurs only when block copolymer is cooled from an ordered melt ($T_{ODT} > T_s$ (starting temperature) $> T_m$)[10] and crystallization temperature is lower than the glass transition temperature of the glassy block ($T_c < T_g$)]. When crystallization temperature is higher than glass transition temperature of the glassy block ($T_c > T_g$), crystallization behaviour is similar to that of rubber/crystalline block copolymer.

The kinetics of crystallization in PE-containing block copolymers have been studied using simultaneous synchrotron SAXS and WAXS[11]. The development of PE crystallites (with an enhanced scattering contrast compared to the initial melt state) was followed via the SAXS invariant using an Avrami equation[12]. The Avrami theory is based on the nucleation and growth of crystallites, and is not specific to polymers. For athermal crystallization it is assumed that all crystal nuclei are formed and start to grow at time $t = 0$, the crystallites then grow at a constant rate until their boundaries meet leading to the formation of spherulites[13]. In thermal crystallization, crystallites are nucleated at a

constant rate in space and time. For athermal and thermal crystallization, the initial radial growth of spherulites occurs during primary crystallization. This is followed by the slower process of secondary crystallization, where crystal thickening behind the crystal front occurs, together with the formation of subsidiary crystal lamellae and an increase in crystal perfection. Nucleation and growth via different mechanisms can be described using the Avrami equation[14];

$$1 - \phi = \exp\left(- kt^n\right)$$

where Φ = the relative degree of crystallinity, $k = (\ln 2)t_{0.5}$ and $t_{0.5}$ = half time of crystallization, n = Avrami exponent which describes the nucleation and crystalline growth mechanism, t = time of crystallization. For the PE-PEE diblocks (and PE homopolymers) studied by them, $n = 3$. This is consistent with the athermal growth of spherulites in three-dimensional space, as usually observed for growth of lamellae in crystallizing polymers. However, it was found that this exponent does not describe the secondary crystallization process[14].
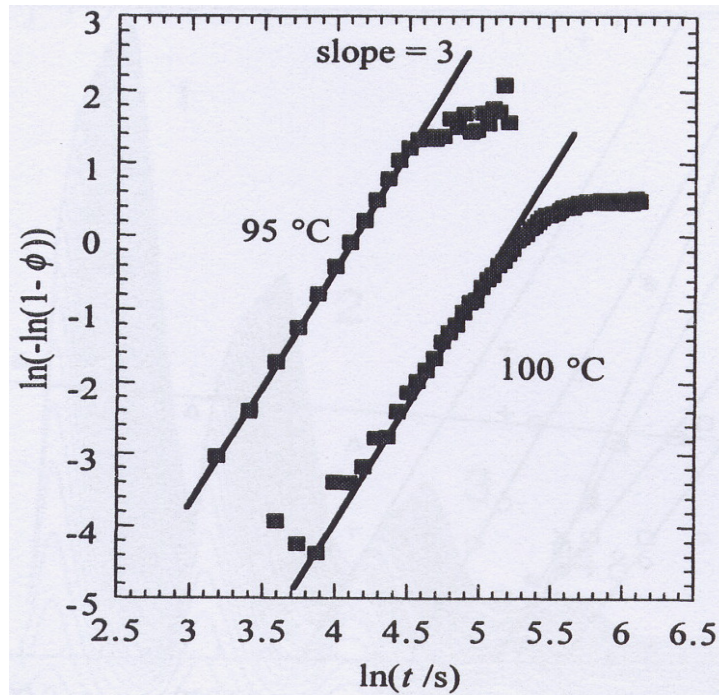
Figure 2.4 : Avrami plots showing the growth of the relative degree of crystallinity (Φ) for a PE-PEE diblock (M_n = 23kgmol^{-1}, f_{PE} = 0.49) at 95^{0}C and 100^{0}C. The double logarithm of the relative degree of crystallinity determined from the SAXS invariant is plotted against the logarithm of the time.

2.3 Orientation in Block Copolymers

In contrast to homopolymers, where folding of chains occurs such that stems are perpendicular to the lamellar interface, parallel orientation has been observed for block copolymers crystallized from the heterogeneous melt. It is not yet clear whether that is always the preferred orientation, or whether

chains can crystallize perpendicular to the lamellar plane, for example when crystallization occurs from the homogeneous melt solution.

Bates and coworkers[15] studied the lamellar orientation of a nearly symmetric amorphous poly(ethylethylene)/poly(ethylene-propylene) (EE/EP) diblock copolymer samples which were textured using large strain dynamic shear. Near the order-disorder transition (ODT) temperature, and at low shear frequencies, the lamellae arrange parallel to the plane of shear, while higher frequency processing leads to lamellae perpendicular to the plane of shear. But at temperatures below the ODT, parallel orientation were obtained at all shearing frequencies.

This results prompted Kofinas and Cohen[16] to inquire the possibility that semicrystalline block copolymer systems might also exhibit perpendicular lamellar morphology under shear. They subjected the samples to a high plane strain compression using a channel die during which was done from a quench to room temperature. It was found that when the diblocks were oriented above the PE melting block (at temperatures below but close to the ODT) at various compression ratios, the lamellae oriented perpendicular to the plane of shear. In other words, the PE crystallized in the pre-existing perpendicular orientation formed in the melt close to the ODT. The lattice unit cell orientation of the crystallized polyethylene chains with respect to the lamellar superstructure was determined and results that the chains were perpendicular to the lamellar normal irrespective of the texturing temperature. In contrast, compression below T_m, caused the lamellae to orient parallel to the plane of shear.
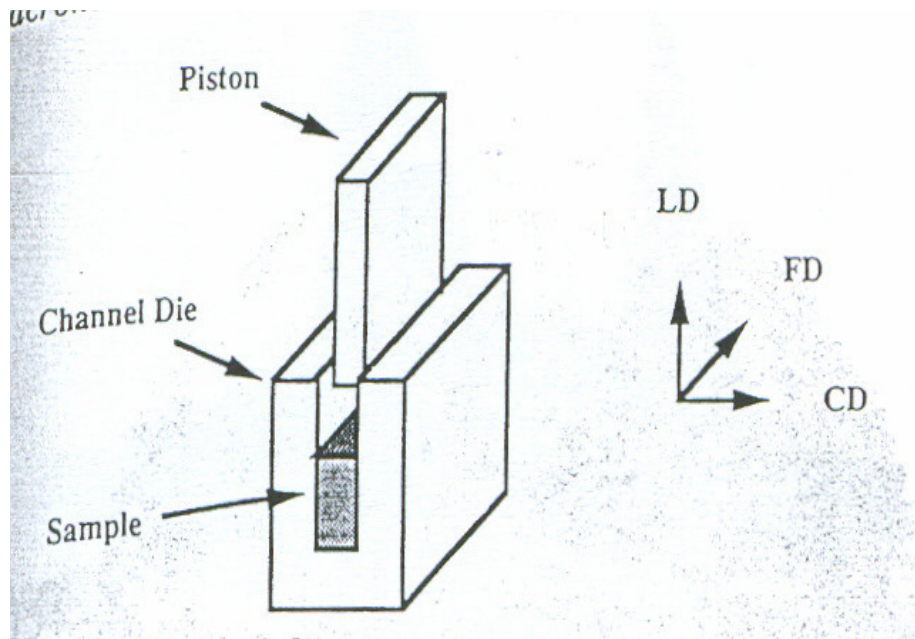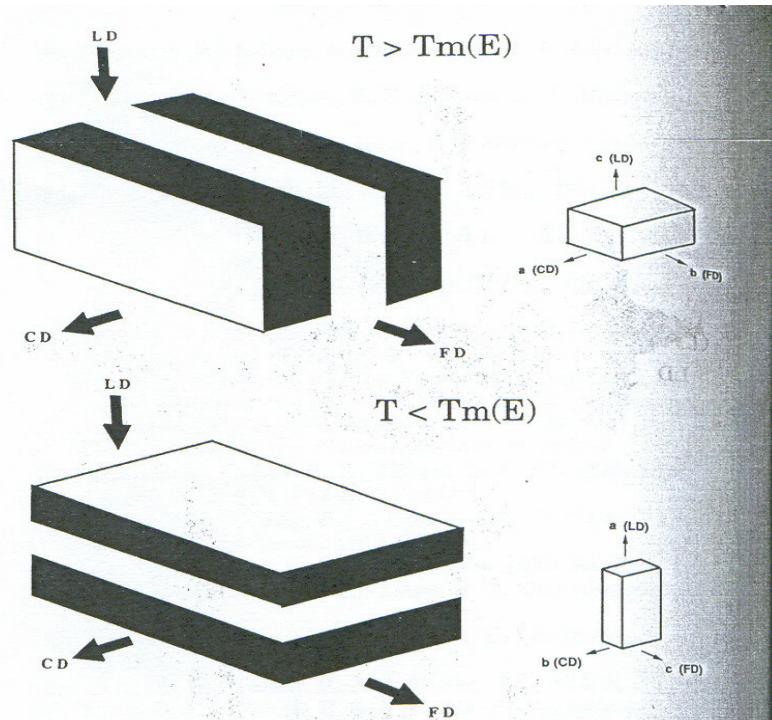

Fig.2.5   Channel Die Apparatus

Fig. 2.6   Sketch of lamella and unit cell orientation in E/EP specimens processed above (a, top) and below (b, bottom) the E block melting point. The insert shows the orientation of the orthorhombic PE unit cell.

Chapter Three –Analysing Techniques

3.1 Small-Angle X-ray Scattering

X-rays are in effect, scattered by the electrons in matter and that interference, or diffraction, occurs between x-rays scattered by electron 'clouds' that surrounds the various atomic centers. In a more general sense, x-ray interference effects result from variations in electron density from one point to another in the material. Because of the reciprocity between interatomic distance and $\sin\theta$ ($n\lambda = 2d$ $\sin\theta$), inhomogeneities of colloidal dimensions generate x-ray scattering and interference effects at very small angles, typically less than 2^0 with the wavelength of Cu$K\alpha$, 1.542Å. It should be emphasized this small-angle scattering has no dependence on the inhomogeneities of atomic dimensions that give rise to the wide-angle diffraction[17]. From the standpoint of the small-angle scattering, the concentrations of electrons on the atomic sites, which constitute the basis for the description of crystal structures, might as well be replaced by continuous distributions of electrons within the unit cells. Only the fluctuations in electron density over much larger distances, typically 30 to 1000 Å, determine the nature of the small-angle scattering. Therefore rather perfect single crystals, pure phases in general, and other homogeneous substances do not scatter x-rays at very small angles.

The two kinds of inhomogeneity that are most likely to be response for small-angle x-ray scattering from solid polymers are (a) alternation of crystalline and amorphous regions, which in general will possess different electronic densities, and (b) the presence of microvoids dispersed throughout the solid polymer matrix. The intensity of small-angle scattering increases with the degree of contrast between the electron density of the two or more kinds of regions that produce the heterogeneity[17]. Thus, it is relatively large for a system of discrete particles separated by interstices or the inverse, a dispersion of micropores in a solid medium, but relatively small for heterogeneous system of crystalline and amorphous regions that differ slightly in density.

The experimental requirements for useful small-angle scattering experiments are very exacting in comparisons with the requirements for wide-angle measurements[17]. This is due, in the first place, to the necessity of measuring the scattered radiation at angles that are very close to the undeviated beam, which in turn requires very sharp collimation of the incident x-ray. In the second place, it is usually necessary to evacuate the apparatus in order to eliminate air-scattered x-rays, which at small angles are of sufficient intensity to distort or mask features of the small-angle scattering emitted by the specimen. Thirdly, for the analysis of diffuse small-angle scattering it is mandatory that wavelengths other that the desired characteristics radiation (for example, Cu$K\alpha$, with λ=1.542Å) be removed by means of crystal monochromator.

3.2 Wide Angle X-rays Scattering

Wide Angle X-ray scattering (WAXS) is used to obtain structural characteristics and to identify powders, thin films, and crystals on the scale of 1 nm or smaller. It can be also used for characterization of polymer crystallinity as well as bulk analysis.

For both experimental and theoretical reasons it is useful to separate x-ray diffraction effects into Small and Wide-angle regions according to the size of the angle of deviation from the direct beam, customarily designated 2θ. In addition to the explanation given above, Small angle diffraction can be referred to the effects observed at an angles smaller than about 2 or 3^0. Wide-angle diffraction encompasses effects that are observed at all larger angles, theoretically extending up to 180^0.
In WAXS, the x-rays are 'reflected' by a set of crystallographic planes in much the same way as light are reflected by a mirror[17].
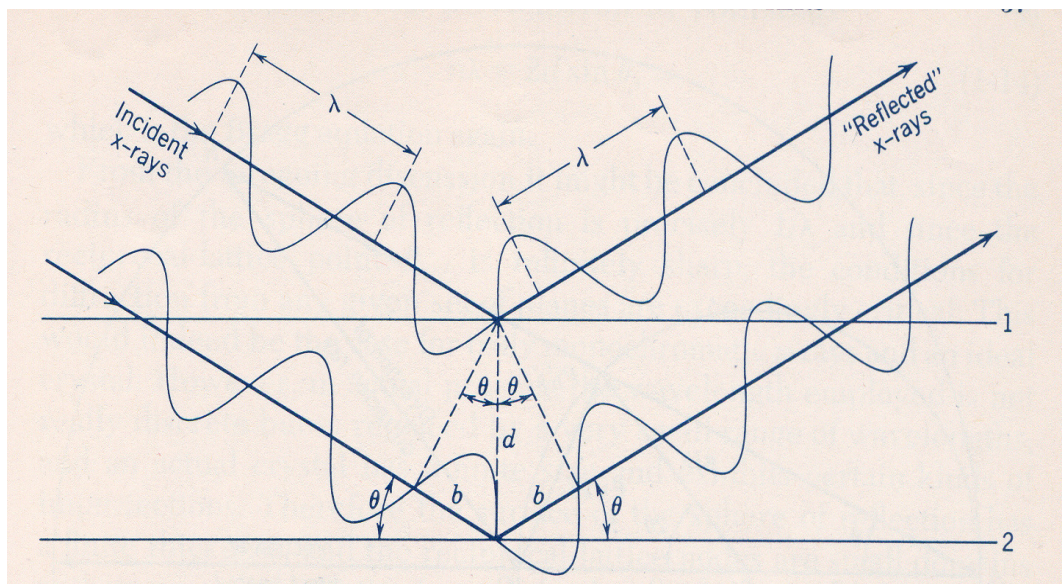
Fig. 3.1   Geometry of Bragg reflection analogy

X-rays of a wavelength, λ, impinging at the angle θ, on two adjacent planes of a set (*hkl*) separated by an interplaner distance d . Reflected x-rays are shown making an angle θ with these planes. The diffenrence in path length between the rays reflected by planes No. 1 and 2 is 2b. The wavelength, the interplaner distance and the one- half the angle of deviation of the diffracted rays are related by the Bragg's equation.

$$n\,\lambda = 2d\sin\theta$$

From the geometry of the figure above, it can be seen that the reflected waves from the two planes will be in phase[17] when

$$n \lambda = 2b = 2d\sin \theta$$

In the illustration of the crystallographic planes, a two-dimensional *ab* lattice of an orthorhombic space is depicted below. From the diagram it is clear that any given set of Miller indeces, *hkl,* (obtained by taking the reciprocal of the unit intercepts and clearing the fractions) refers not to just one plane but rather to a family of parallel plane that permeates the entire crystal and is characterized by a particular interplaner spacing *d(hkl)*[17]. It can be seen from the figure below how planes of simple indeces, such as (100) and (010) are more densely populated with lattice points than planes of more complicated indices (for example, (210) and (230)).
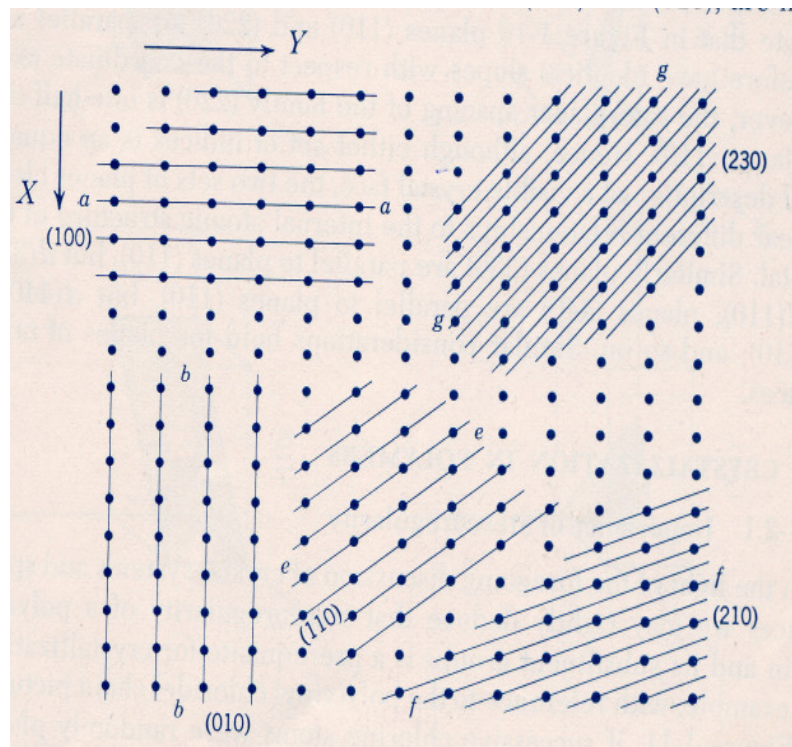
Fig. 3.2 Plane traces on an *ab* net of an orthorhombic space lattice

The formulas for the interplaner spacing in relation with the unit cell dimensions (a, b, c) of several crystal systems are as follows[17].

12

Cubic system;

$$d = \frac{a}{\sqrt{h^2 + k^2 + l^2}}$$

Tetragonal system;

$$d = \left(\frac{h^2}{a^2} + \frac{k^2}{a^2} + \frac{l^2}{c^2} \right)^{-\frac{1}{2}}$$

Orthorhombic system;

$$d = \left(\frac{h^2}{a^2} + \frac{k^2}{b^2} + \frac{l^2}{c^2} \right)^{-\frac{1}{2}}$$

Hexagonal system, hexagonal indexing:

$$d = \left[\frac{4}{3a^2} \left(h^2 + k^2 + hk \right) + \frac{l^2}{c^2} \right]^{-\frac{1}{2}}$$

WAXS offers the most fundamental method, against which the results based on other techniques may be compared. This is so because the basic concept of the crystalline and amorphous phases involves the degree of order of packing of atoms and segments in space, which can be revealed most unambiguously by the study of x-ray diffraction patterns. An amorphous material possessing only a liquidlike short range order produces a broad, diffuse scattering, with the peak intensity centered on the so called amorphous halo.

A perfect crystalline material, on the other hand, produces diffraction only at sharply defined Bragg angles. In reality, the crystalline order in polymers is never perfect and is disturbed, for example, by the presence of lattice imperfections or finite size crystalline regions and, as a result, the Bragg diffractions may be broadened into peaks having finite widths. Nevertheless, the diffraction patterns obtainable from the crystalline and amorphous phases are in general clearly distinguishable. The x-ray diffraction pattern obtainable from a semicrystalline polymer consists of a superposition of crystalline and amorphous patterns, as shown in Figure below.
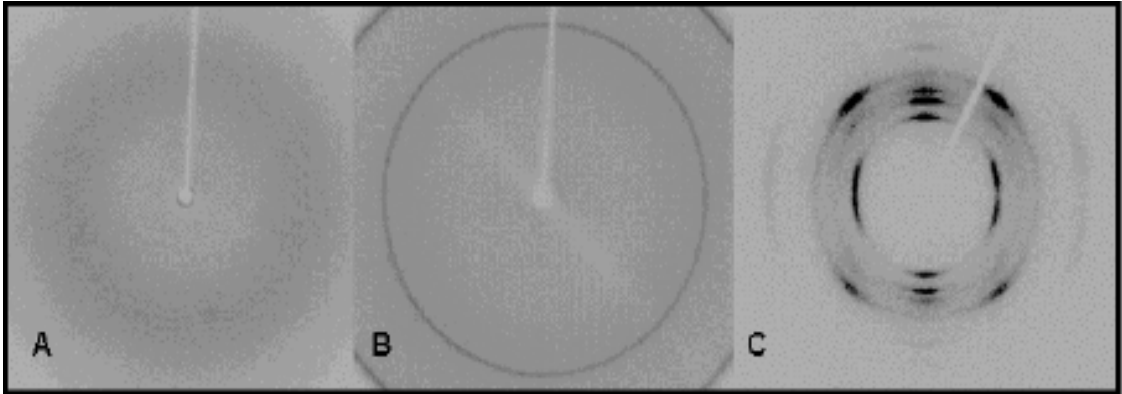
Figure 3.3: A) amorphous scattering, B) unoriented polycrystalline scattering, C) oriented polycrystalline and amorphous scattering.

As shown in Figure 3.3 , X-ray scattering from amorphous material produces a "halo" of intensity, which when integrated obtains a broad, low-intensity "hump." X-ray scattering from a crystalline material produces well-defined spots or rings which integrate to sharp, higher-intensity peaks[18].
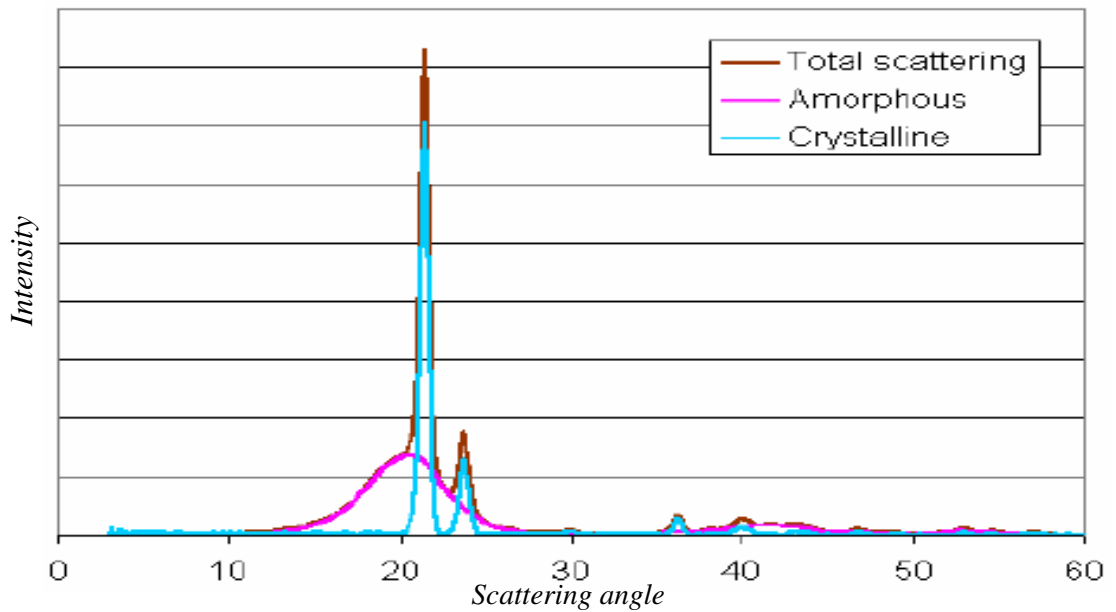

Figure 3.4: A typical WAXS Curve

From the area under the curve method the crystallinity can be given as:

$$\text{Cryst}_{\text{XRD-HW}} = \text{Area}_{\text{cryst}} / (\text{Area}_{\text{cryst}} + 1.2977 * \text{Area}_{\text{amorph}})$$

3.3 FT-Rheology

The FT-Rheology can be understood as a theoretically and experimentally simple method to describe time-dependent and nonlinear rheology phenomena[19].
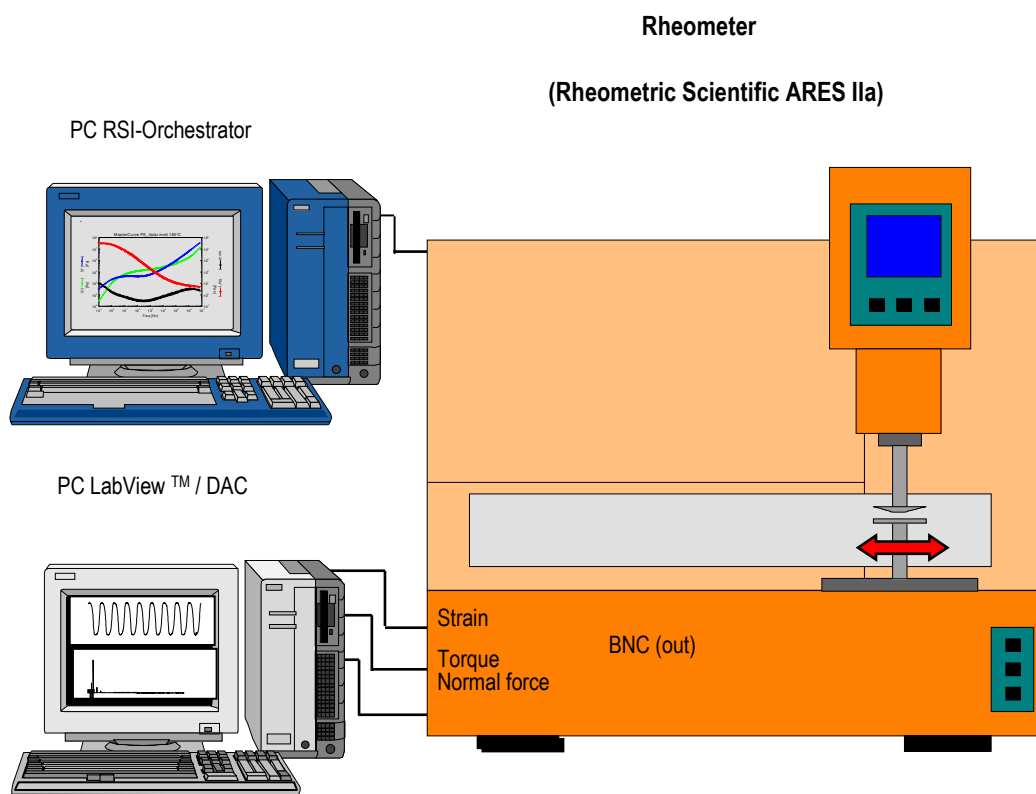
Fig. 3.5; Experimental setup used for all rheological experiments. To the Rheometric Scientific ARES rheometer one additional PC's is connected via shielded BNC-type cables to minimise the electronic noise level.

In general, the Rheometric Scientific ARES rheometer as pictured above is used in the shear orientation experiments. This rheometer is of CR-type (REF). Where a defined strain (rate) is applied and the resulting torge is measured. The rheometer is equipped with a standard 2KFRTN1 torque transducer. Raw data are measured and Fourier transformed using home-written LabVIEW 5.1 program[20]. Usually, the sample prepared by heating close to the order-disorder temperature while compressing the sample between Teflon-covered plates to achieve a dense packing without air bubbles. Pieces of about 0.5mm thick of the sample would then be mounted on the rheometer. Macroscopic orientation is generally obtained from the disordered melt after the shearing.
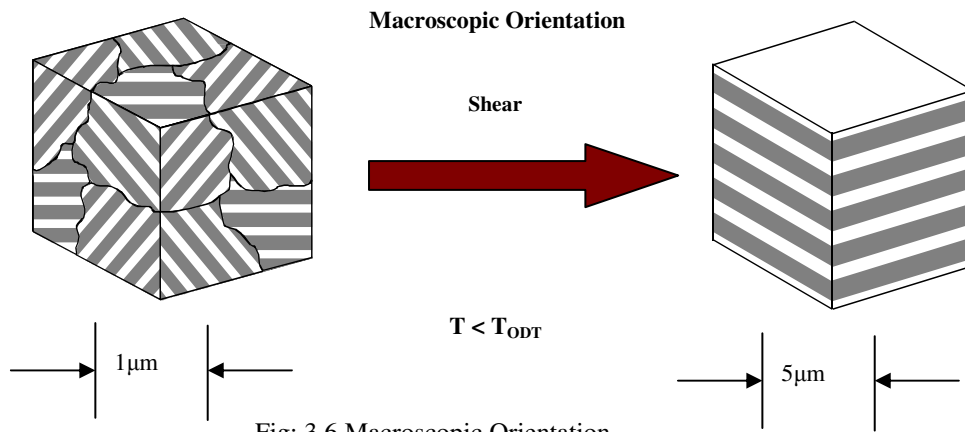
Fig: 3.6 Macroscopic Orientation

The preferred orientation in the course of the orientation process depends strongly on the experimental parameters. For LAOS experiments with parallel plate geometries it has been shown that the four most important parameters are frequency (ω_1), strain amplitude (γ_0), temperature (T), and the duration of shear. For temperatures close to the order-disorder transition temperature (T_{ODT}) and for long shear times (approximately 10 h), the preferred orientations detected are either parallel or perpendicular[21].
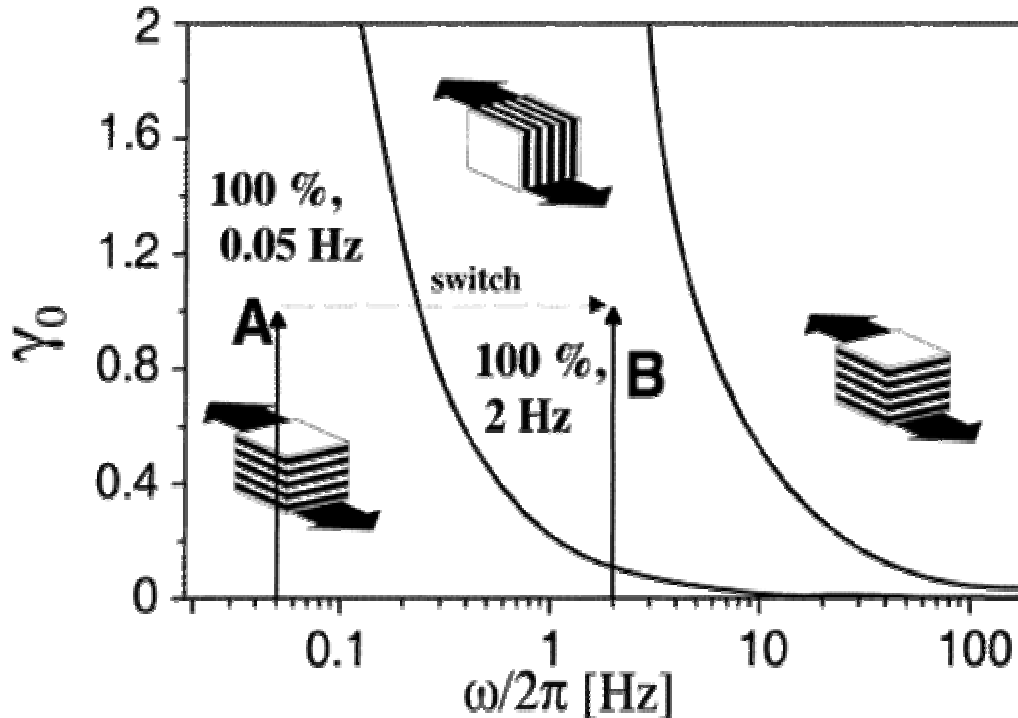
Fig. 3.7 Schematic orientation diagram of the stable macroscopic orientation of a lamellar PS-*b*-PI under LAOS conditions. The solid arrows show the experimental conditions used for this study.

The orientation process is normally analysed by 2-dimensional small-angle x-ray scattering (2D SAXS) measurements to get a X-ray pattern for all three Cartesian directions of the sample. Typical diagrams obtainable can be seen below. Figure 3.8 shows a 2D SAXS patterns of a radial and tangential stripe of PS-*b*-PI samples at γ_0 = 0.5 in three Cartesian directions (normal, radial, and tangential) after (a) 10 h of prealignment and after (b) 20 h of total experimental time to investigate the presence of (a) parallel and (b) perpendicular orientation of the lamellae[21].
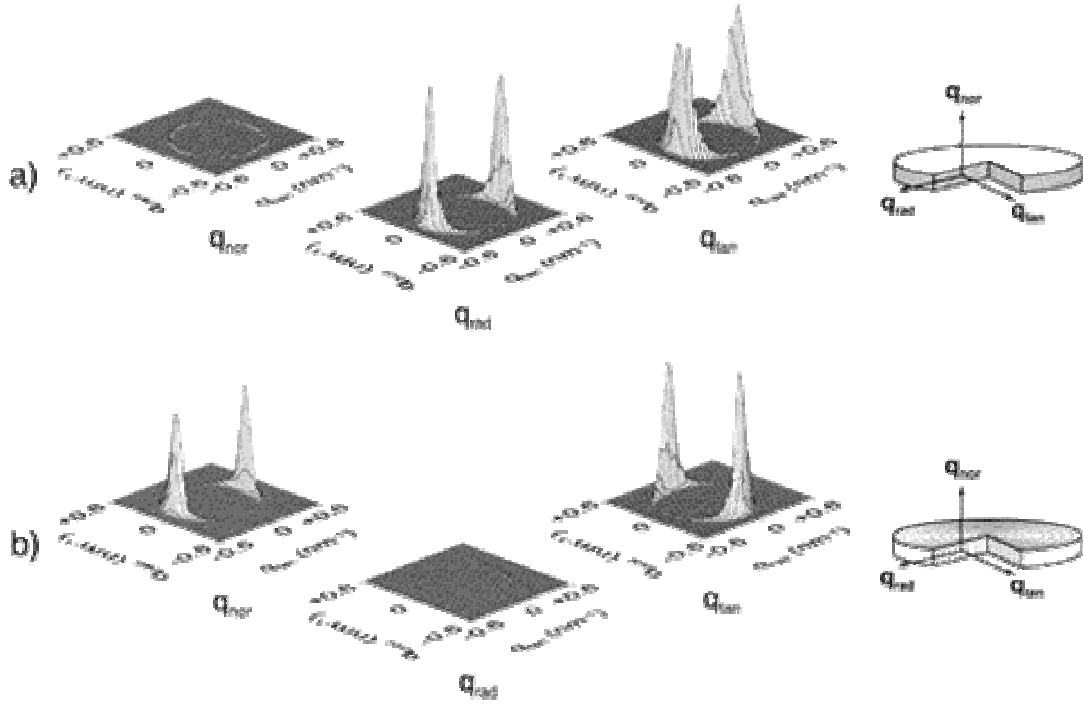
Fig 3.8:   2D Waxs Pattern

For quantitative interpretation of the 2D SAXS data, the order parameters $<P_2>$ of the different samples can be calculated from the X-ray figures in the three directions especially the radial direction. This order parameter can be characterized between 0.1 and 0.6 (i.e. from low to high orientation)and the equation can be given by;

$$\langle P_2(\cos \chi) \rangle = \frac{\int_0^\pi S(\chi) \left[\frac{1}{2} (3 \cos^2 \chi - 1) \right] \sin \chi d\chi}{\int_0^\pi S(\chi) \sin \chi d\chi}$$

Where S(χ) is the scattering intensity depending on the scattering angle χ .

17

3.4 Raman Spectroscopy

Raman Spectroscopy is based on the Raman effect, which is the inelastic scattering of photons by molecules. The Raman effect comprises a very small fraction, about 1 in 10^7, of the incident photons. In Raman scattering, the energies of the incident and scattered photons are different. The energy of the scattered radiation is less than the incident radiation for the Stokes line and the energy of the scattered radiation is more than the incident radiation for the anti-Stokes line[22]. Raman spectrum can be obtained from molecules which have a change in Polarizability but not change in dipoles as in the case of Infrared Spectroscopy.

Raman spectroscopy can give useful information on the tacticity, crystallinity and orientation of a polymer. Different tactic forms of a polymer frequency give rise to easily distinguishable Raman spectra. Broad Raman bands of low peak intensity are characteristic of materials which have a low stereochemical purity, such as atactic samples or those with mixed head-to-head and head-to-tail fragments. The FT Raman spetrum of isotactic polystyrene is distinguishable from that of the atactic isomer[23]. Highly ordered species give rise to characteristically sharp and hence intense Raman spectral bands compared with those of disordered material. For the disordered material, the spectral bands broadened and new bands due to gauche linkages are observed. The tendency of amorphous materials to be poor Raman scatters and hence produce weak spectra further emphasizes the difference between the two spectra.

Conventional Raman spectroscopy can be used to determine the lamellar thickness of polymer crystal, whether they be independent as in solution-crystallized materials or stacked as in melt-crystallized case. This method relies on recording the frequencies of longitudinal acoustic modes (LAMs). The frequency of these modes is inversely proportional to lamellar thickness. The most LA modes lies in the frequency range of $\Delta \upsilon = 5\text{-}30 \text{cm}^{-1}$, making it impossible to record using current FT Raman instruments and filter technology[23].

In *C-C Stretching* and in general, for a perfect crystalline linear alkanes with C-chains = 24 possessing orthorhombic chain packing show two broad bands, representing asymmetric ($\Delta \dot{\upsilon}_{as}$) and symmetric ($\Delta \dot{\upsilon}_{s}$) stretching vibrations at 1063 and 1131 cm^{-1}, respectively[24]. For a hexagonal system of alkanes, these vibrations appears at the same bands.

Chapter Four- Experimental Analysis

4.1 Synthesis of Poly(styrene-*block*-ODMA) Copolymer

The Poly(styrene-*block*-ODMA) diblock copolymer was synthesized via anionic polymerization. For initiation, *sec*-butyllithium was added to a solution of styrene in THF. Reaction conditions are T=-78^{0}C/t = 1h for Styrene; T=-78^{0}C/t = 1h for n-OctaDecylMA. DPE plus s-BuLi was added to a THF in storage flask and then the styrene which the initiator followed. Later the n-OctadecylMa was then added. The sample was precipitated into H2O/CH$_3$OH mixture. There was a stable orange colour during the polymerization but red colour appeared after DPE addition. Adding of n-OctaDecylMA results in termination of crystals, no reaction, only after allowing the temperature to rise to -10^{0}C, solution became colourless.

Poly(styrene-block-octadecylmethacrylate) copolymer
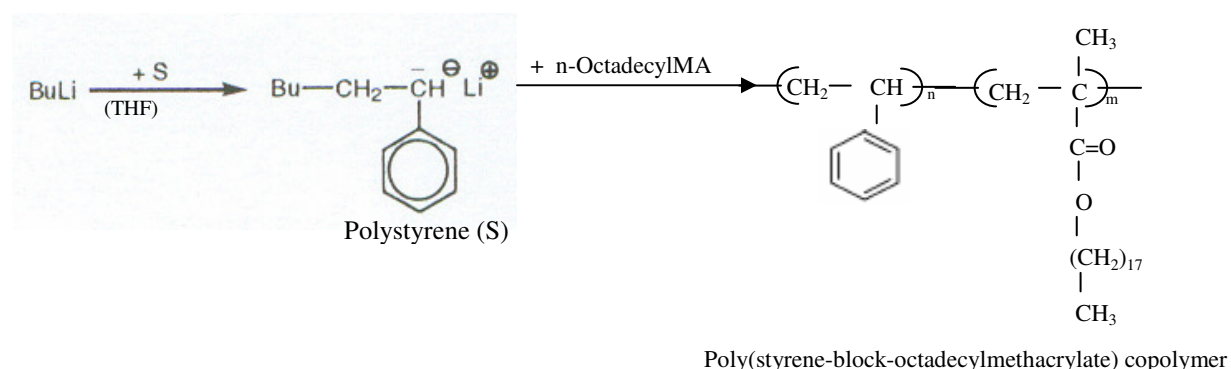
4.2. Parameters of (Poly(styrene-*block*-ODMA) Copolymer)

The poly(styrene-*block*-ODMA) copolymer has the following existing parameters.

	Homo ODMA 27	**Cylinder B 224/24**	**Lamella B 154/25**
$\boldsymbol{\Phi}$ ODMA	1	0.18	0.39
M_n (Kg/mol)	9.0	27.6	24.4
M_w/M_n	2.1	1.1	1.1
N ODMA	27	12	25
Ns	-	224	154
$\Delta H^{*,\#}$ (J/g)	56	28	45
$D^{\#}$ (mol%)	31	15	25

$T_{on,m}{}^{\#}$ (^{o}C)	32	11	28
$T_{on,c}{}^{\#}$ (^{o}C)	25	11	22
Δ_{Cp} (PS) (J/gK)	-	0.22	0.13
N_{Avrami} (InIn-plot)	3.8	0.70	2.8

Where Φ = Volume fraction , *D = Degree of Crystallinity = $\Delta H / \Delta HCH_{18}H_{38}$ related to PODMA content; $^{\#}$ Heating rate 10K/min.

4.3 Preparation of a Microphase-Separated Sample

The original Poly(styrene-block-octadecylmethacrylate) copolymer is in a powered form which is not phase separated. The sample was annealed at a temperature of $150^{0}C$ for 24 hours under vacuum leading to the formation of the microphase separated sample.

4.4 Decomposition Temperature

The decomposition temperatures for the Lamella and Cylindrical samples were found to be around 262.14 ^{0}C and $272.95^{0}C$ respectively which were obtained from a Thermo Gravimetric Analysis (TGA) measurements. This can be seen on the two graphs below.
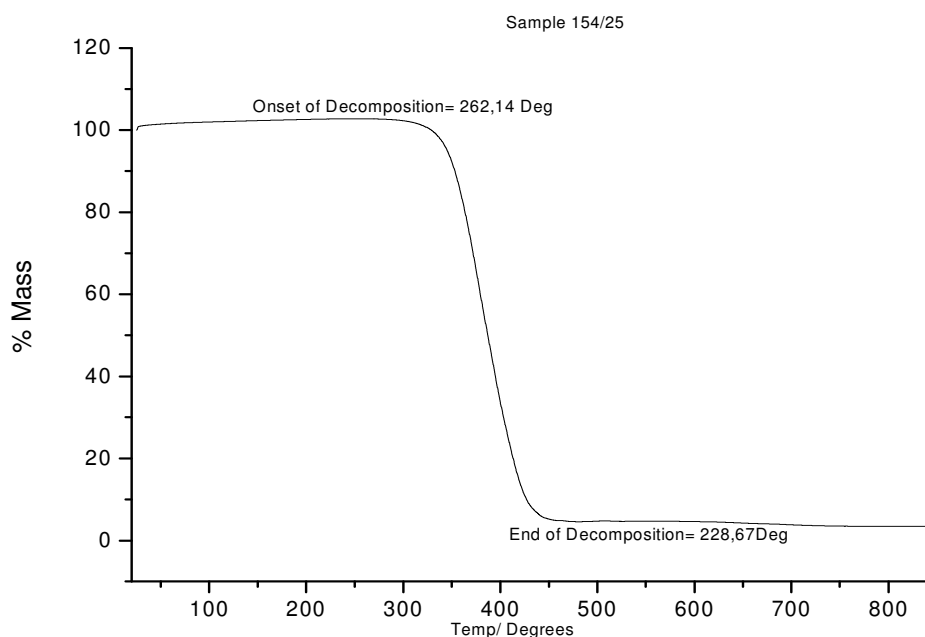
Fig 4.1 Decomposition Temperature Graph for Lamella sample

Sample 224/12
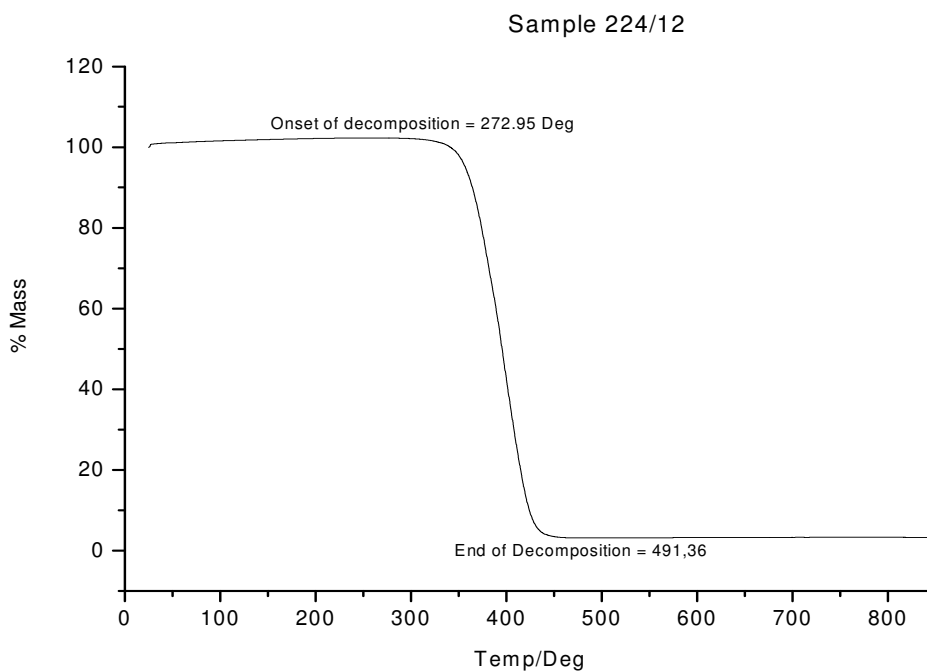
Fig 4.2 Decomposition Temperature Graph for Cylindrical Sample

4.5 Common Solvent for the Two Blocks

Three solvents were used for the investigation. These are THF, 1,4 Dioxane and Toulene. This is because they were very good solvents for the lower side chain methacrylates. The THF and 1,4 Dioxane gave a clear solution while Toulene did not dissolve completely. Hence, the first two were selected.

4.6 SAXS and WAXS Data

a) Analysis of SAXS Data: SAXS measurements were performed for the two samples and the following graphs obtained.

(A)
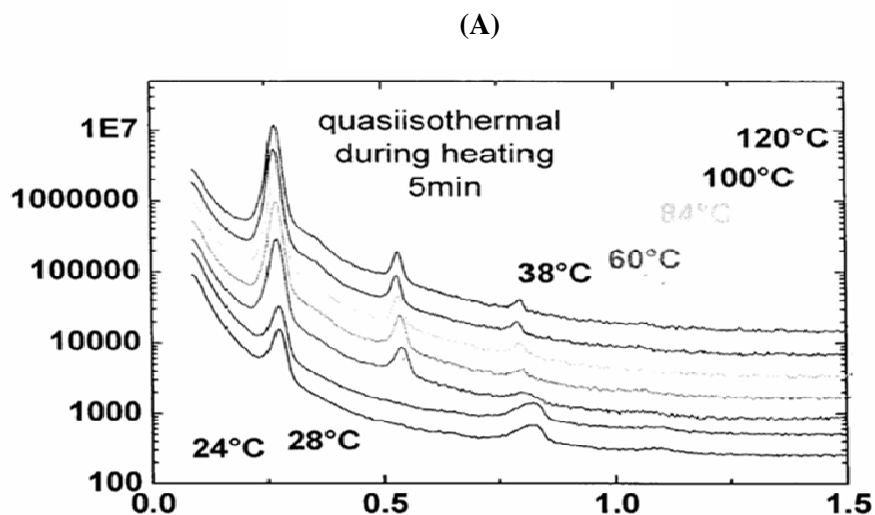
Fig. 4.2 SAXS Measurements for the PS-b-PODMA, $f_{PODMA}= 0.39$

(B)
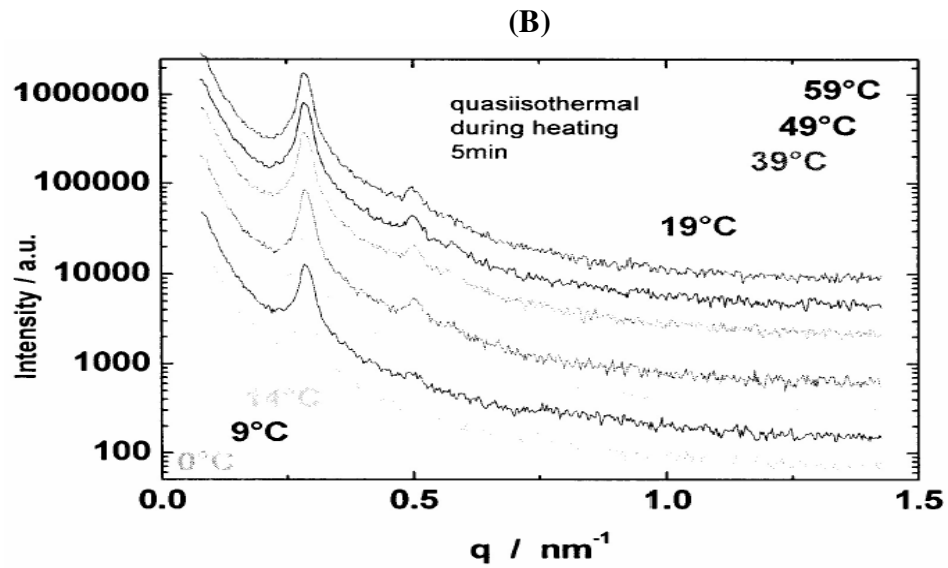
Fig. 4.2 SAXS Measurements for the PS-b-PODMA, $f_{PODMA}= 0.18$

The alternating long period of crystalline and amorphous layer has been evident approximately $q = 0.265 \pm 0.005 nm^{-1}$ corresponding to a structural period of about $\underline{\boldsymbol{d_{struct.}} \approx \textbf{237Å}}$ (d = 2π / q). In the graph (A), there is an appearance of a new peak after the melting and this is due to change in electron density (about 15%) within the system. There is also an increase in the intensity of these peaks with the temperature. From the two graphs, the following models were proposed based on the SAXS graph.

Lamella Sample (154/25)   **Cylindrical Sample (224/12)**
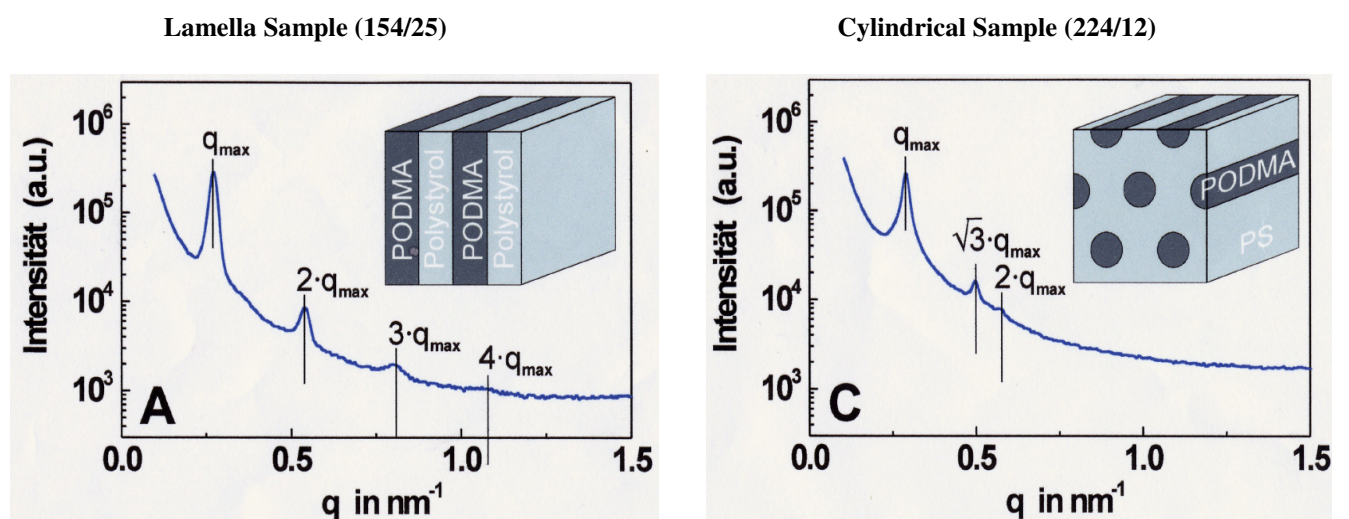
Fig. 4.4 : Proposed Models for both samples

b). Analysis of WAXS DATA: Wide angle X-ray graphs were obtained from the two block copolymers and also the homopolymers using the D500 WAXS machine ($\lambda = 1.54\text{Å}$). For the block copolymers, there was isothermal measurements from room temperature to a temperature of 50^{0}C, cooled down to -30^{0}C and then heated slowly back to room temperature.
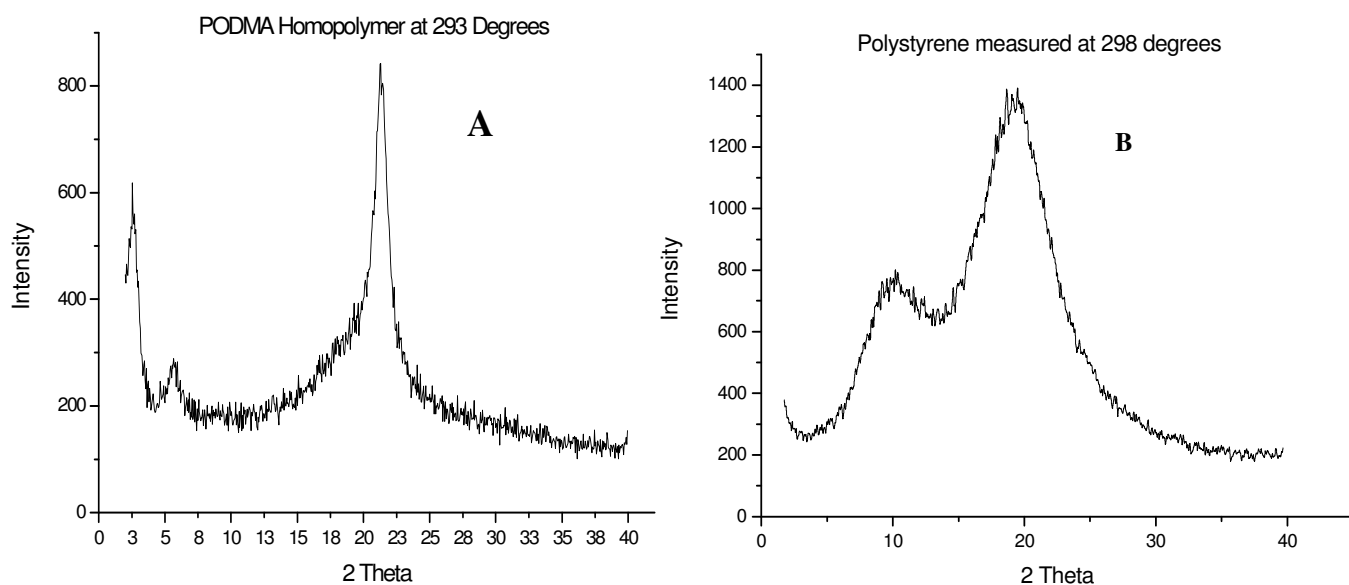
Fig. 4.5: (a) WAXS diagrams for PODMA Homopolymer (N=27) and (b) for Polystyrene Homopolymer
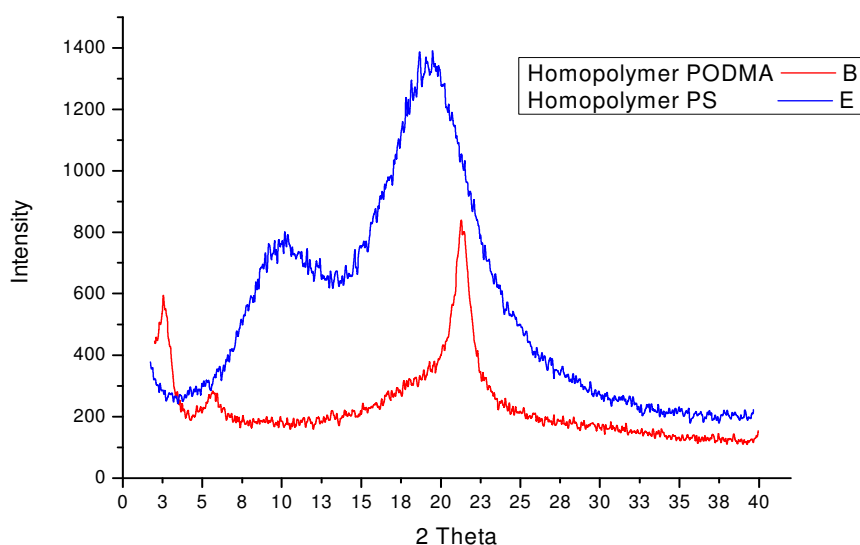
Fig. 4.6: Overall WAXS diagram for PODMA & Polystyrene Homopolymers
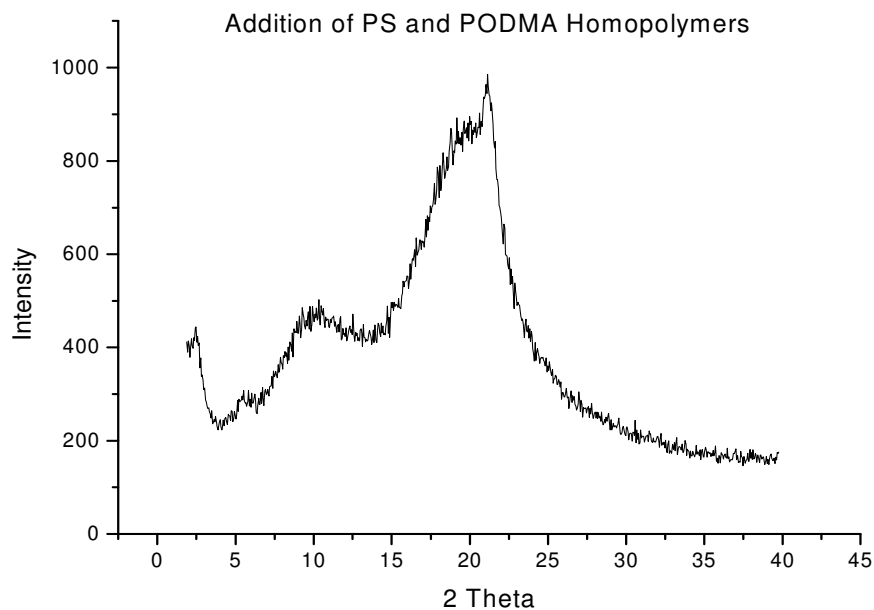
Fig. 4.7   Addition of PS and PODMA Homopolymers

There was only one peak at $2\theta = 21.5$ corresponding to a bragg's spacing d = 4.1Å in the case of the PODMA homopolymer. The first peak of this homopolymer is also at $2\theta = 3$ which gave a $\underline{d_b \approx 29.4\text{Å}}$ corresponding to backbone to backbone distance. The middle peak of the PODMA is at $2\theta = 6$ given **d = 14.7Å.** The polystyrene graph can be seen to have a higher amorphous peak at $2\theta = 19.2$ and the other peak is at $2\theta = 9.8$. These graphs will be used to evaluate the following WAXS graphs of the block copolymers.

Isothermal WAXS Measurements of Block Copolymer (Lamellar Structure)
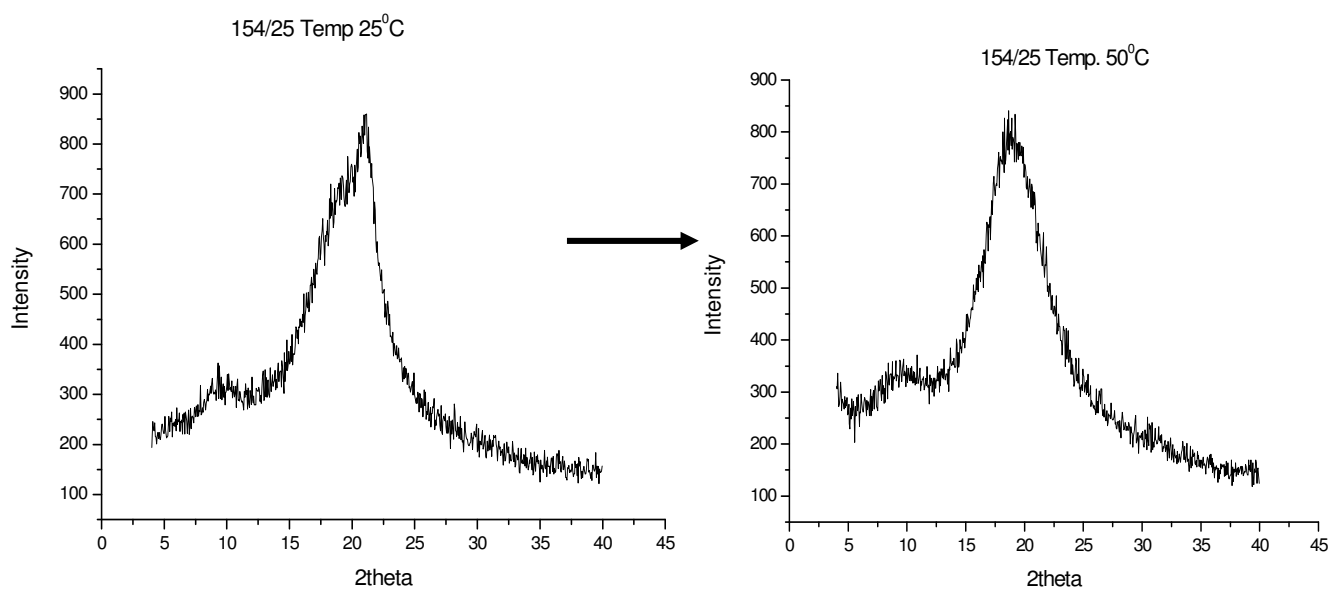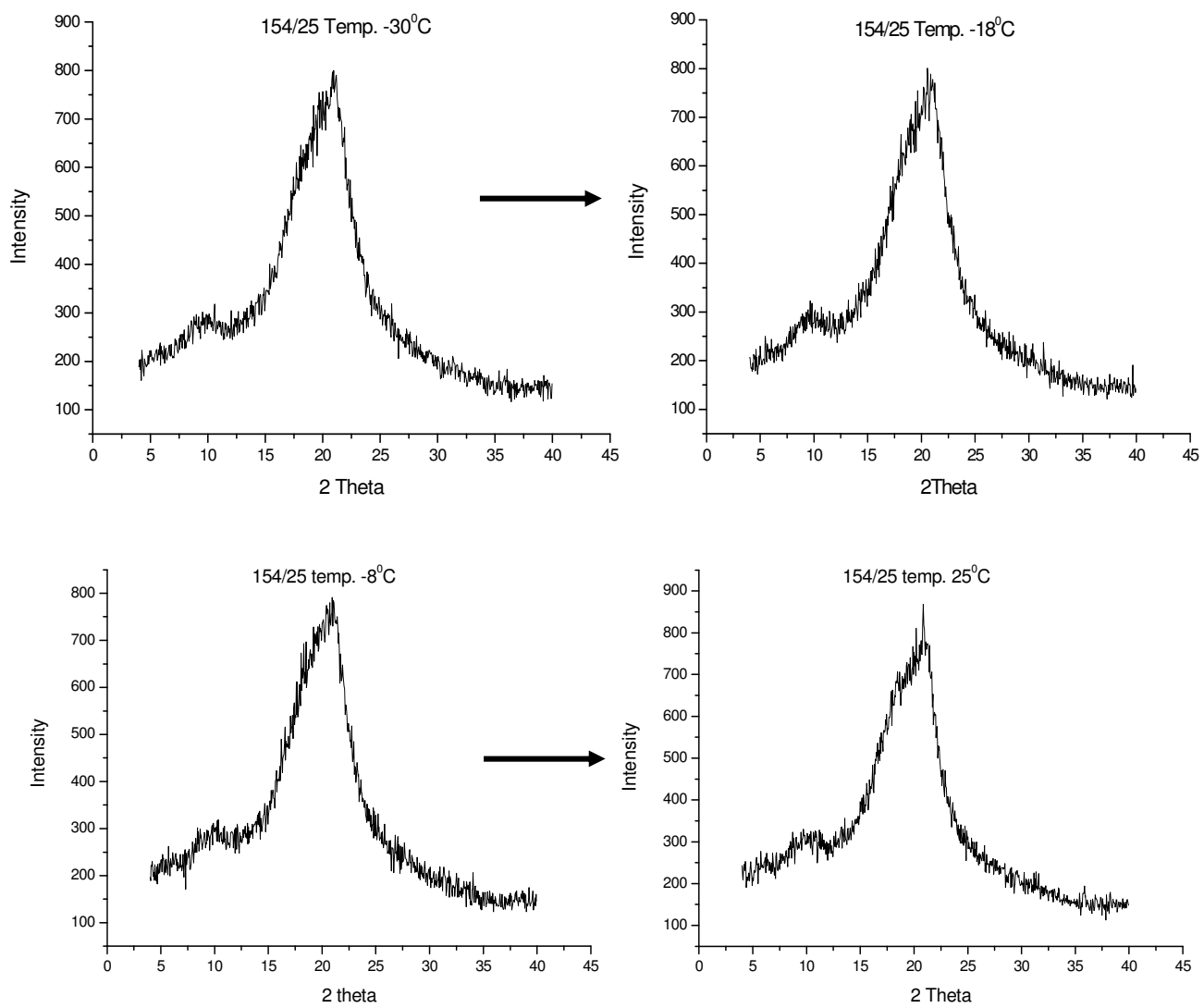
Fig.4.8: WAXS diagrams for lamellar structure PS-b-PODMA at different temperatures
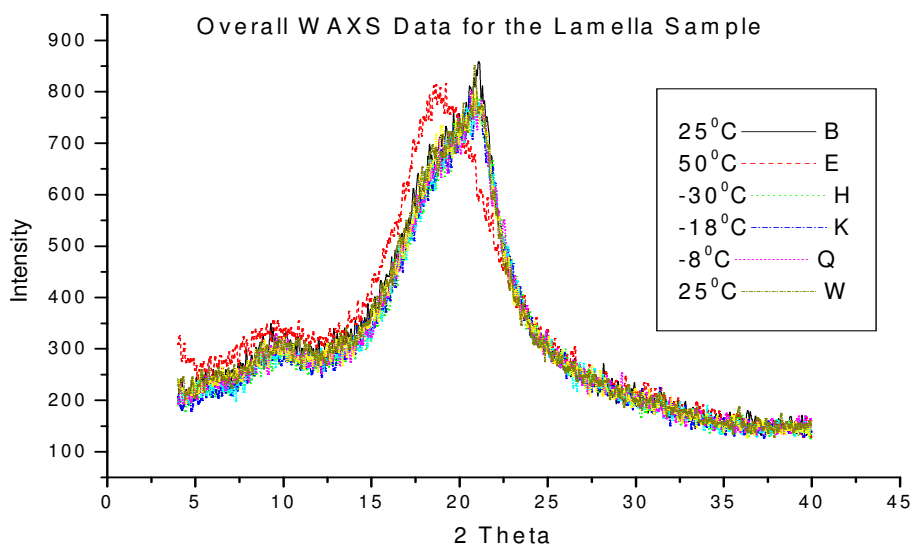
Fig. 4.9: Overall WAXS diagram for Lamella structure PS-PODMA

In this block copolymer sample, and at room temperature, there was a sharp peak on top of the amorphous peak of as shown above. The peaks fitted well with the Lorentz function.
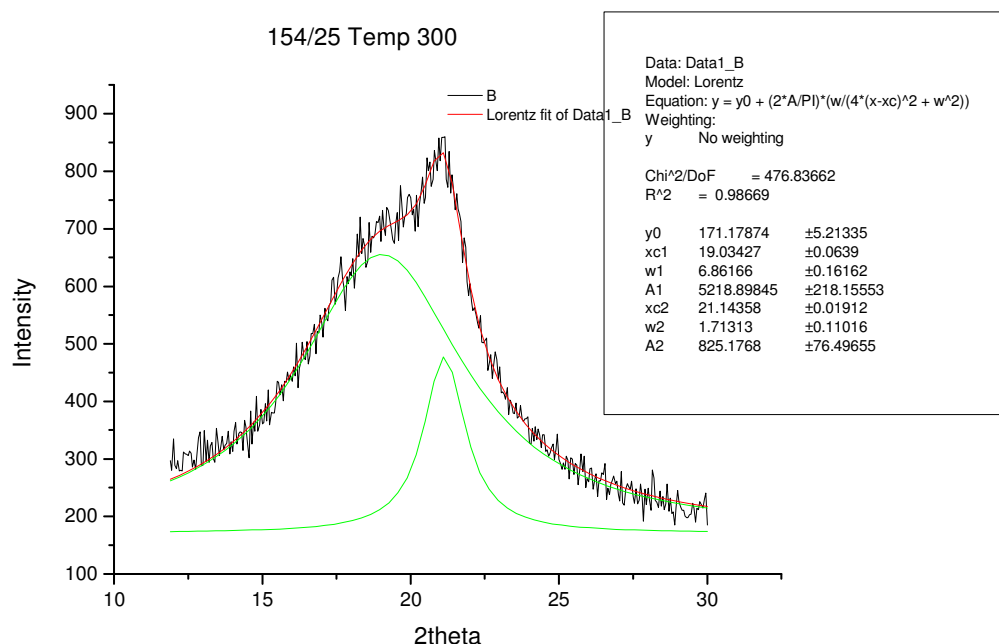
Fig. 4.10 Lorentz function fitting of the Peaks

From the fitting parameters, the amorphous peak was found to be around $2\theta = 19$ degree while the crystalline peak at $2\theta = 21.1$ degree almost the same as the figures for the homopolymers. The amorphous Polystyrene homopolymer data was again subtracted from the block copolymer measured at 50^0C and -30^0C which gave the following peaks. The subtracted crystalline graph fitted best with the Lorentz function.
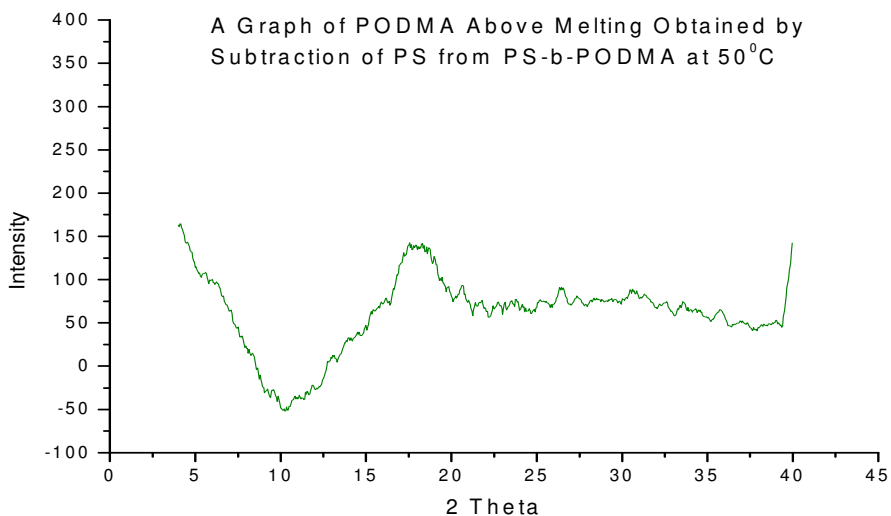
Fig. 4.11; Subtraction of PS from the block copolymer at 50^0C
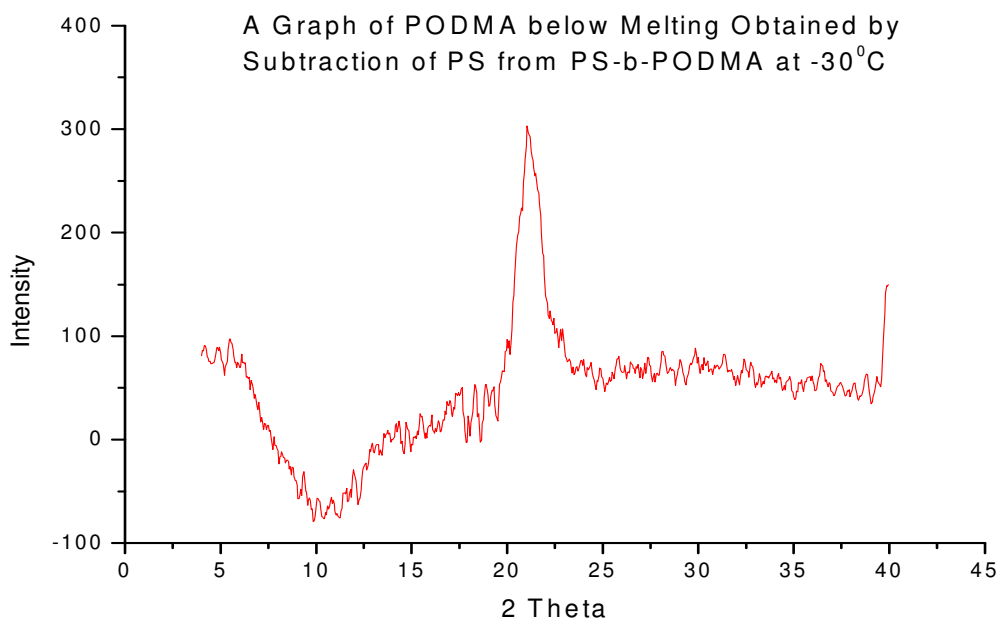
Fig. 4.12; Subtraction of PS from the block copolymer at -30^{0}C

Data: Smoothed3_Data1B
Model: Lorentz

Chi^2 = 1769.91894
R^2 = 0.52173

|		
y0	32.08024	±1.78118
xc	21.23643	±0.03397
w	1.43003	±0.10249
A	593.5585	±32.03556
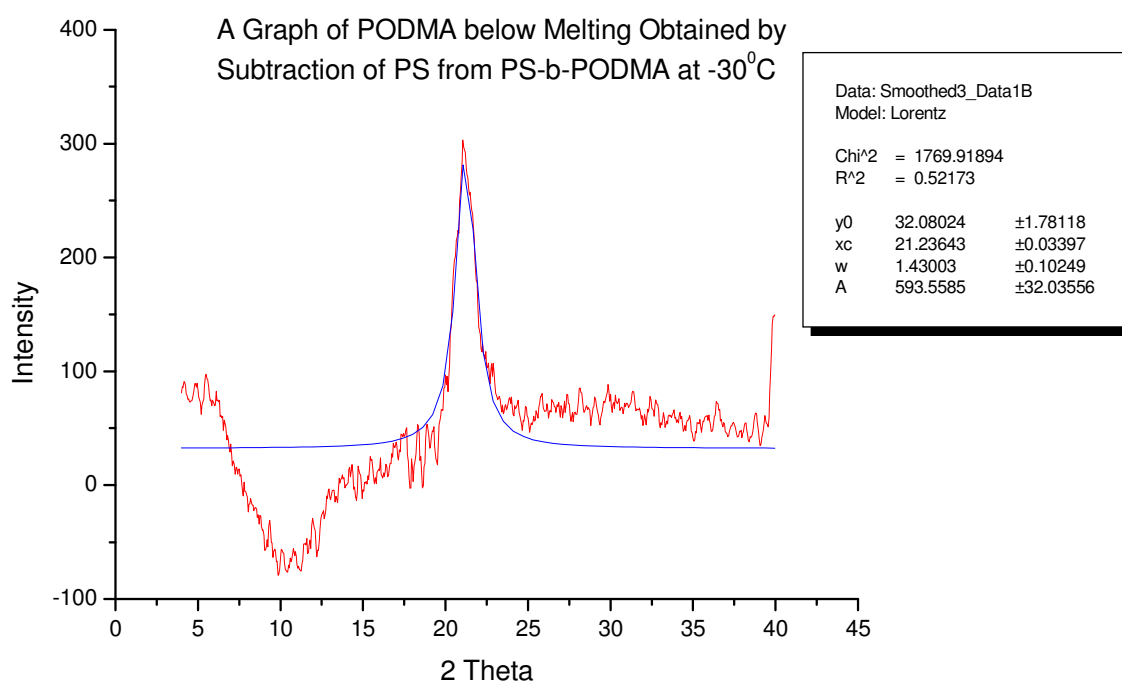
Fig. 4.13; Fitting of Subtracted Curve at -30^{0}C

The analysis of the peaks revealed that the sharp crystalline peak at the top of the amorphous peak is at a approximately $2\theta = 21.2$ given a bragg's spacing of **_d ≈ 4.2Å_** (d = 1.54Å / 2sin(θ/2)). The amorphous peak which was evident after melting of the crystalline peak was at $2\theta = 19.2$

27

corresponding to the Polystyrene peak. The middle peak of the block copolymer represents the first peak of the Polystyrene as seen on the graph of Polystyrene homopolymer.

The same heating process was perfumed to the Cylindrical (224/12) PS-PODMA sample. There was no significant change in the graphs at a temperature T = 50°C. This is because the composition of the PODMA is lower in this case and crystallinity is low. The obtained graphs illustrate the situation.

Isothermal WAXS Measurements of Block Copolymer (Cylindrical Structure)
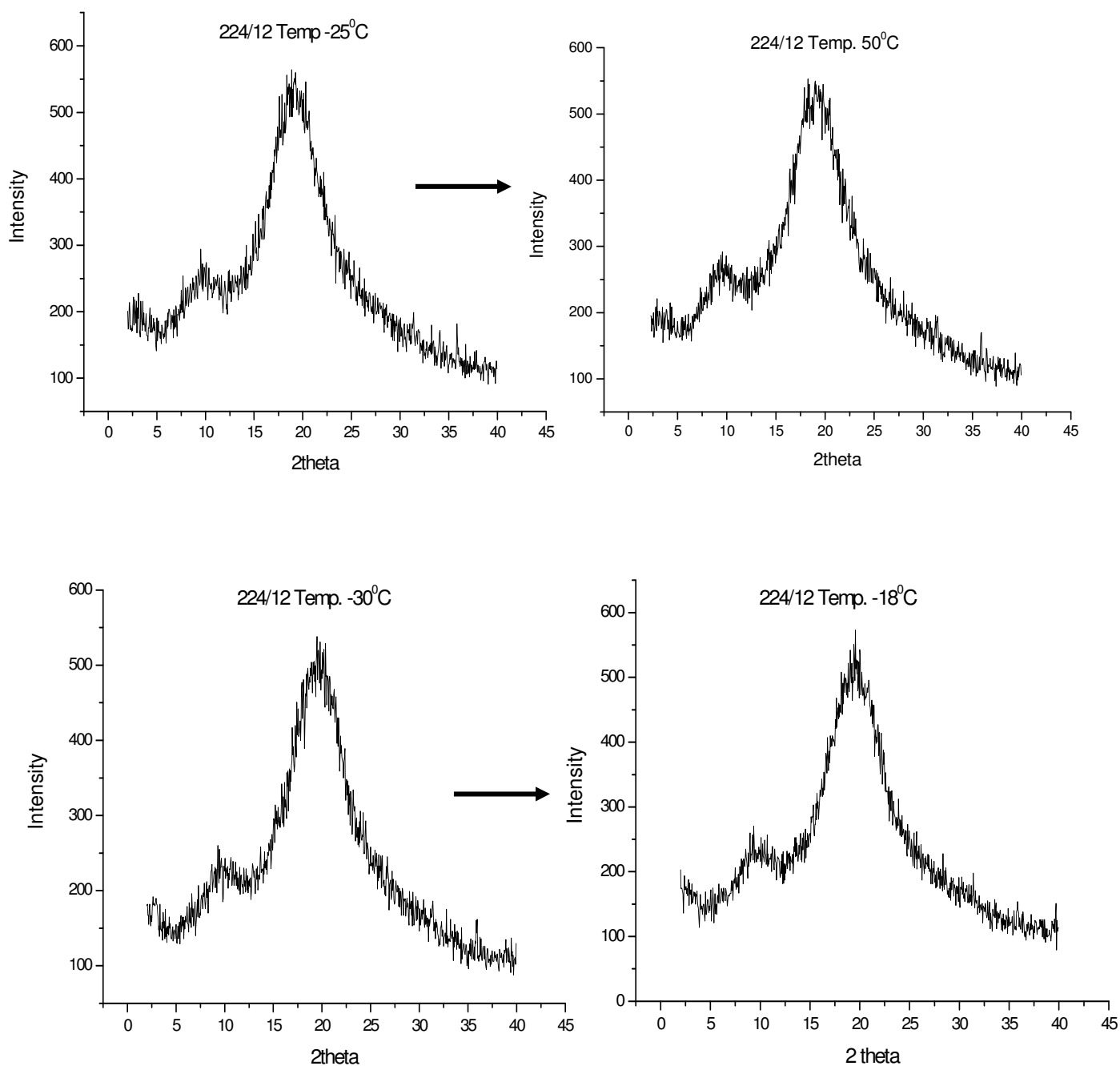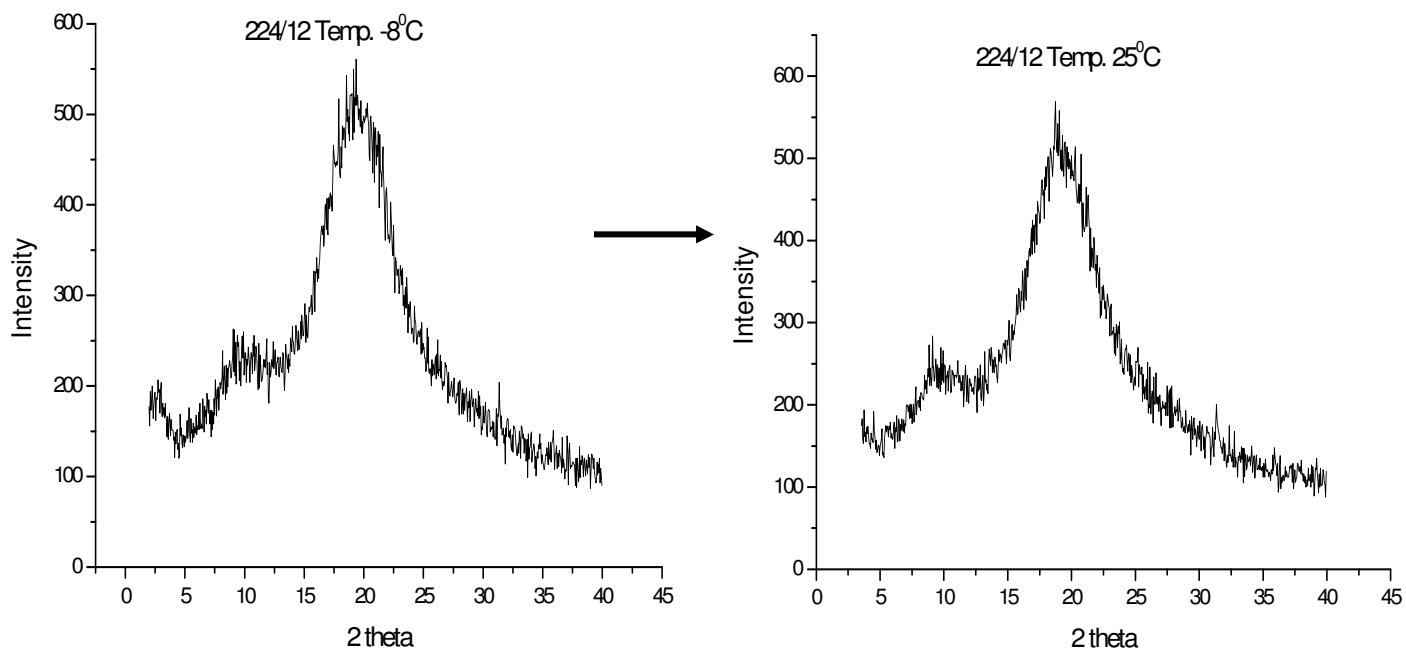
Fig. 4.14: WAXS diagrams for Cylindrical Structure PS-PODMA samples at different temperatures
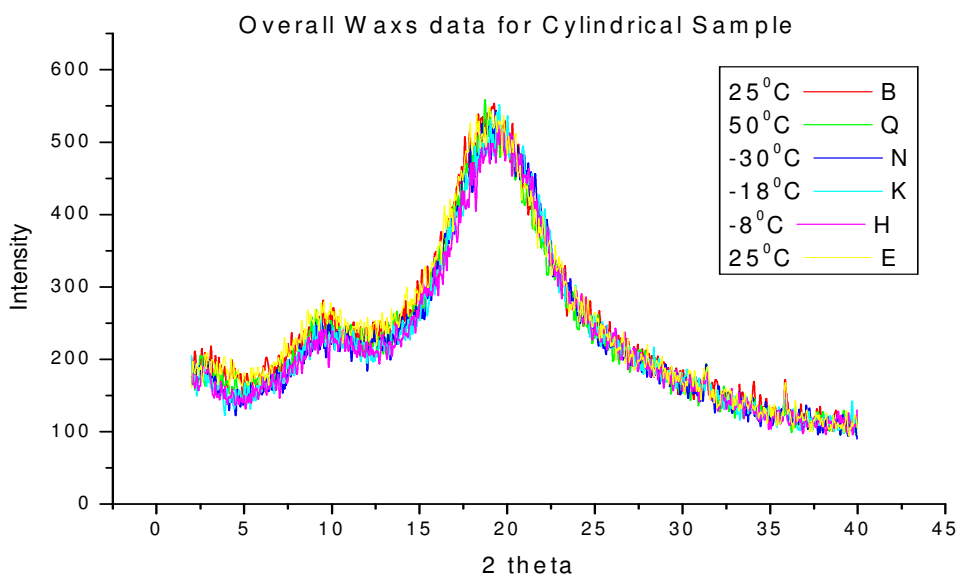
Fig. 4.15: Overall WAXS diagram for Cylindrical structure PS-PODMA
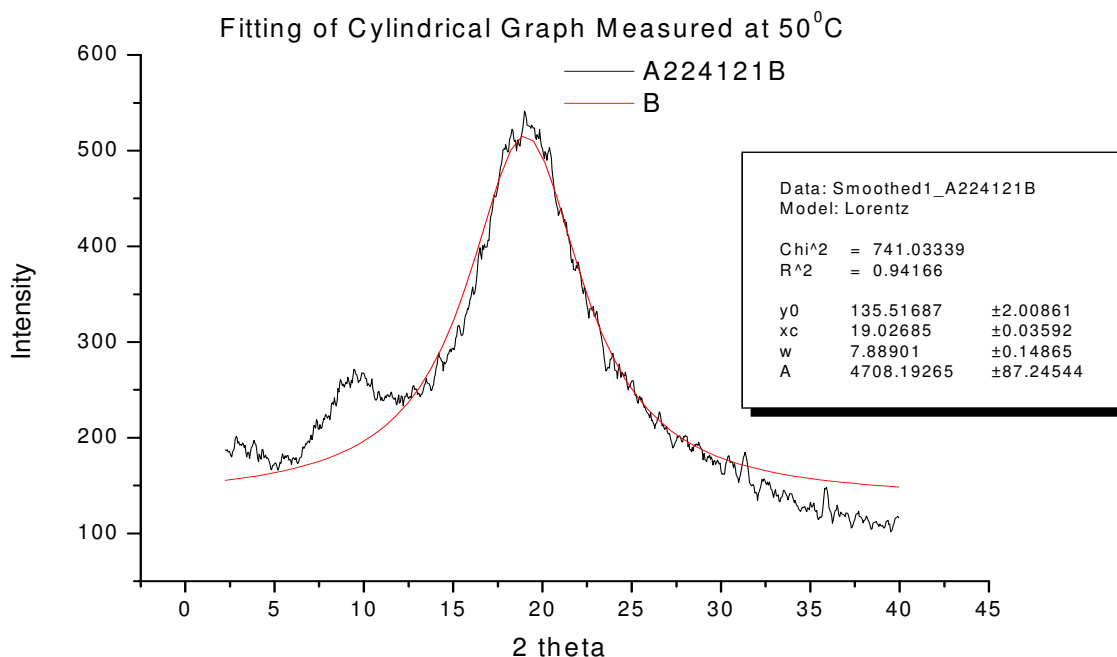
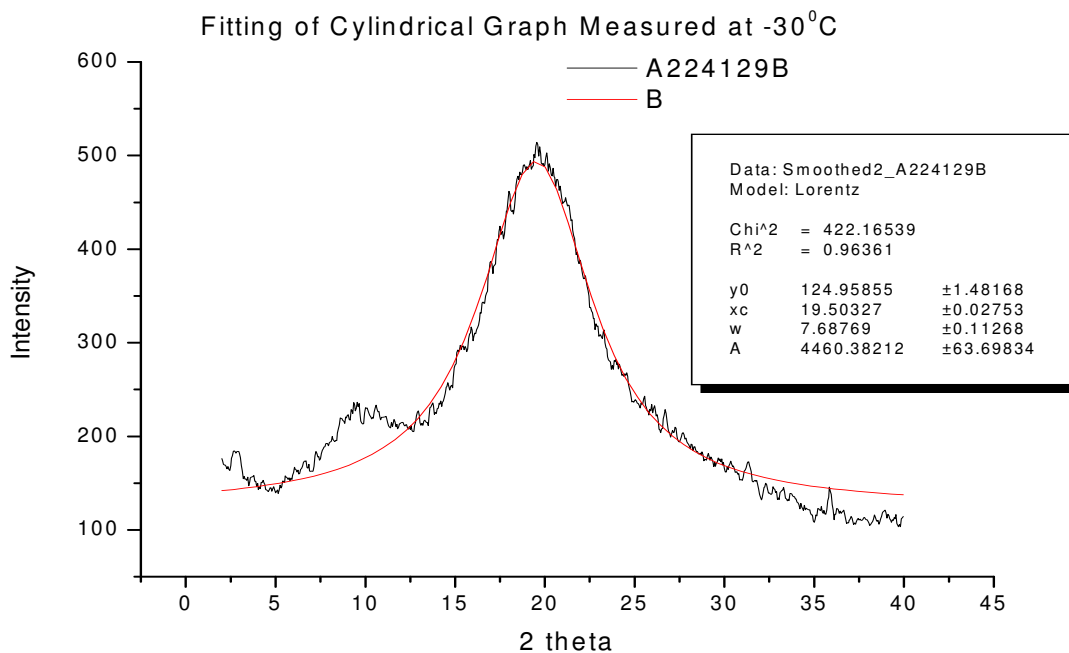Fig. 4.16 ; Fitting of the Cylindrical WAXS Measurement at 50^{0}C

Fig. 4.17 ; Fitting of the Cylindrical WAXS Measurement at -30^{0}C

In this case, the amorphous phase is more dominant in the system. The highest amorphous peak at a temperature of 50^{0}C shows that the PODMA phase has melted and hence shifted to the lower angles close to the polystyrene peak. At a lower temperature (-30^{0}C), the peak shifts more to the higher angles by $2\theta = 21.2$.

4.7 The Order-Disorder Transition Temperature (ODT)

The order-disorder transition temperature was verified by Isothermal SAXS measurements up to a temperature close to the decomposition temperatures for the two samples. The following graphs were obtained. All measurements were performed on a sample prepared in a capillary.
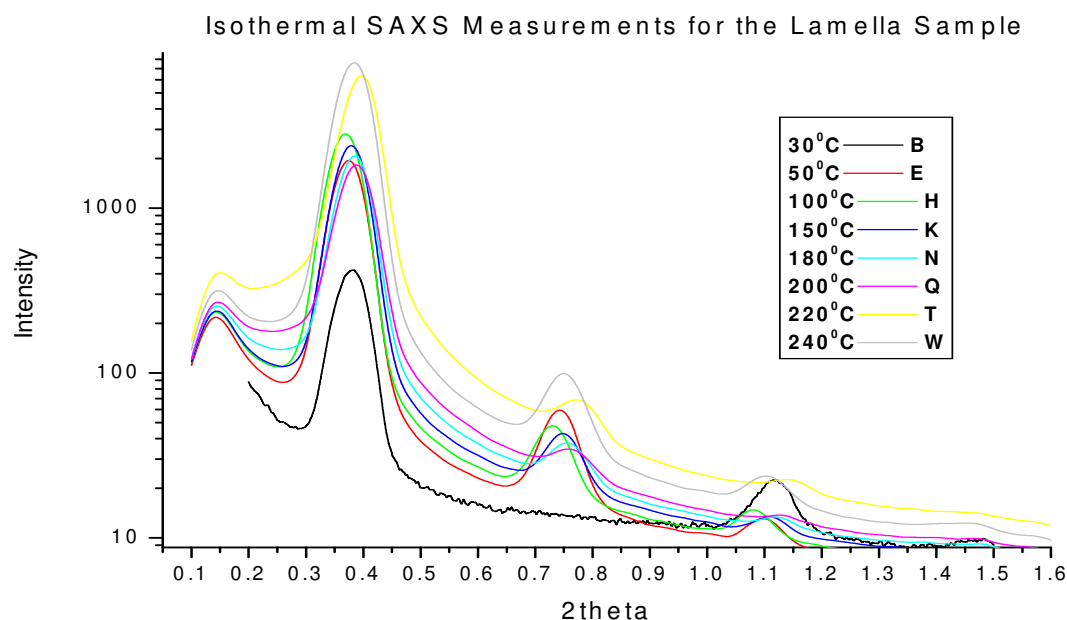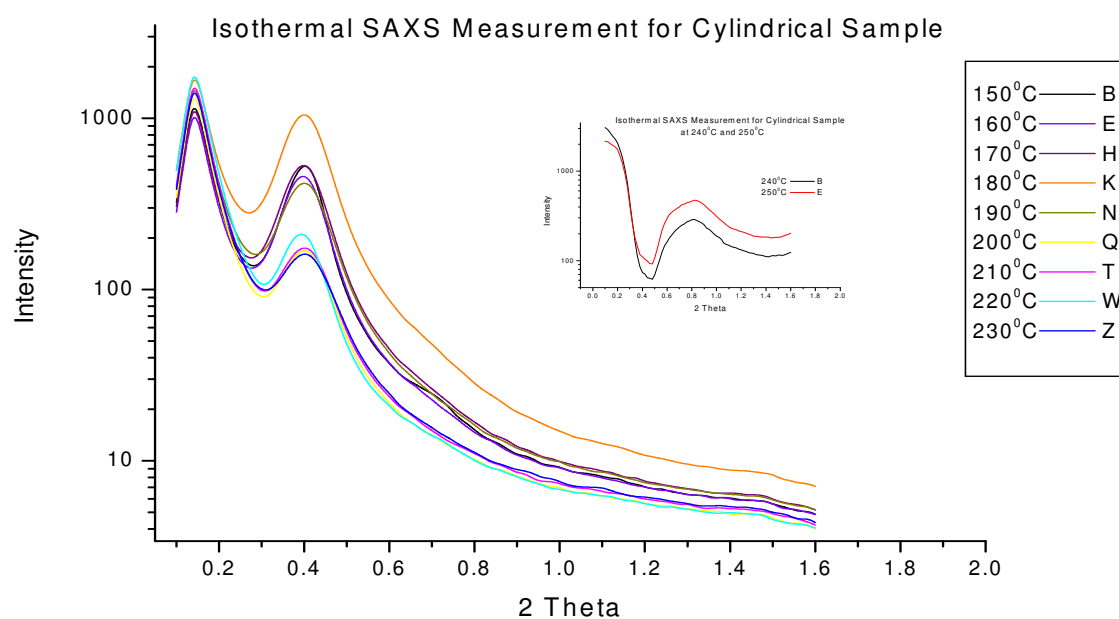
Fig. 4.18: SAXS Data for ODT

Fig. 4.19: SAXS Data for ODT

There was no significant changes in the peaks as observed in the two graphs for both samples. In the lamella graph, one peak appeared after the melting temperature of the PODMA which also was seen in the other SAXS measurement. However, the peaks did not show any change in the higher temperatures (close decomposition temperature). In the Cylindrical graph, there was also no change in the peaks up to a temperature of 230^0C. At temperatures of 240^0C and 250^0C, there were structural decomposition and the sample was destroyed. This has been shown in the insert of the above data.

Usually, the sample prepared by heated close to the order-disorder temperature while compressing the sample between Teflon-covered plates to achieve a dense packing without air bubbles. Pieces of about 0.5mm thick of the sample would then be mounted on the spectrometer. Macroscopic orientation is generally obtained from the disordered melt after the shearing.

4.8 Shear Orientation

For the orientation experiments, a Rheometrics ARES rheometer as described in the early on was used. The sample was prepared by heating it above the glass transition temperature ($T_{g,PS}$ + 30^0C) while compressing it for about thirty (30) minutes under a pressure of 10kN between Teflon-covered plates to achieve a dense packing without bubbles. The large-amplitude oscillatory shear (LAOS) experiments were performed in a plate of plate geometry 8mm with a gap of 0.9mm. A frequency of 0.1 Hz and a temperature of 130^0C was used to measure the strain dependent shear modulus and also the third harmonic. This was done to verify the strain limit to achieve nonlinearity.
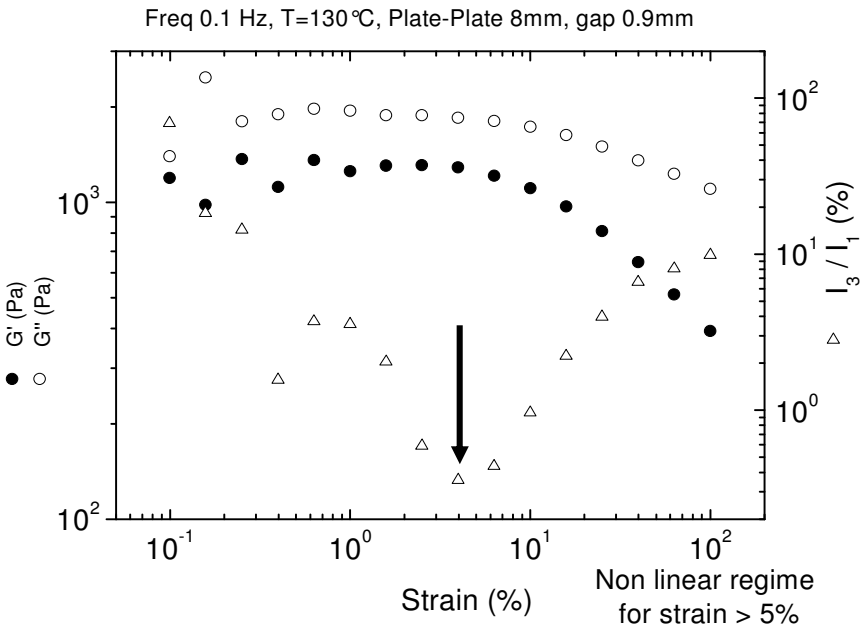
Fig. 4.20 Strain dependent of shear modulus and Third harmonic

The strain amplitude limit to achieve nonlinearity was found to be around 5% and this has been indicated to start from the arrow shown on the graph. This strain amplitude limit was used to verify the time dependent shear modules as shown below.

Again, to quantify the time evolution of the shear orientation process, the shear modulus was plotted against time applying a strain $\gamma_0 = 5\%$ taken from the first experiment. As shown on the diagram below, there was a monotonic decrease in both the real and imaginary part of the shear modulus. This indicates that a good orientation process can be achieve in our sample.

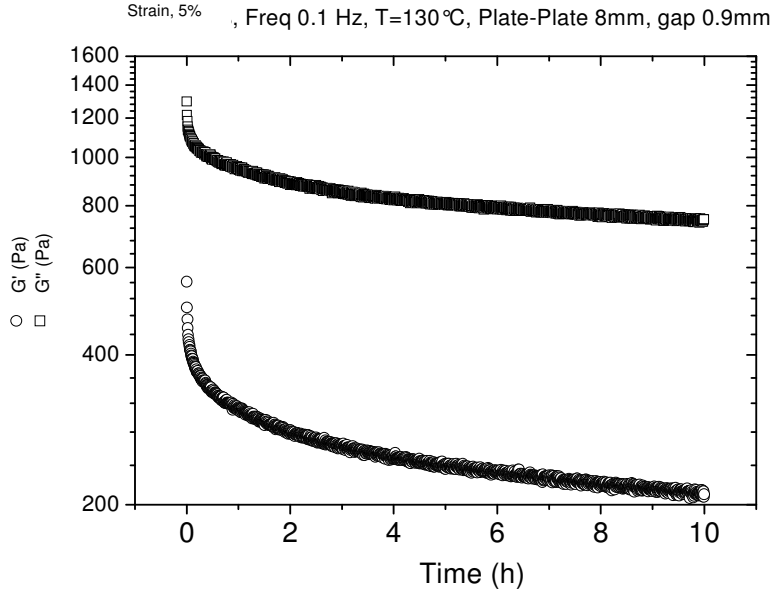Strain, 5% , Freq 0.1 Hz, T=130 °C, Plate-Plate 8mm, gap 0.9mm

Fig. 4.21: Time evolution of the shear orientation process

The orientation process was performed using the above conditions with a typical orientation time of about t = 10 hours. The time dependent third harmonic shown below.

.
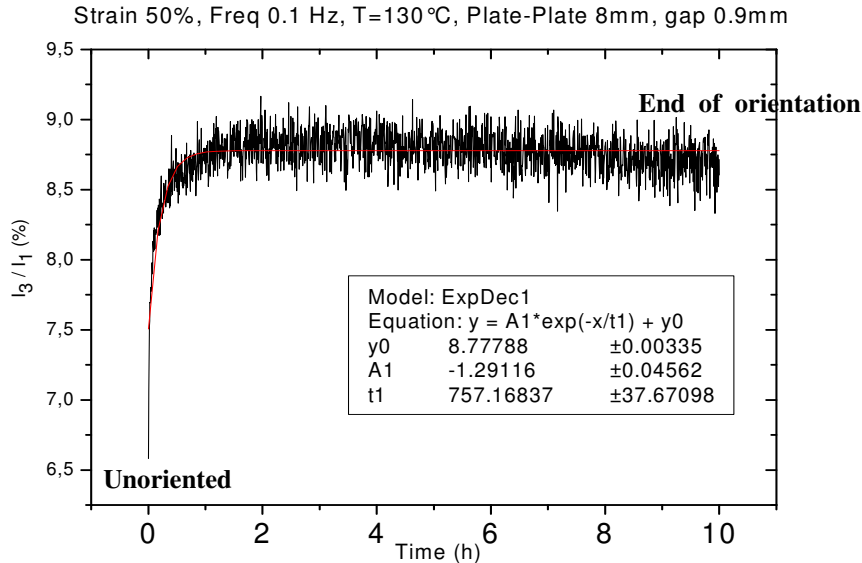
Strain 50%, Freq 0.1 Hz, T=130 °C, Plate-Plate 8mm, gap 0.9mm

Model: ExpDec1
Equation: y = A1*exp(-x/t1) + y0
y0   8.77788   ±0.00335
A1   -1.29116   ±0.04562
t1   757.16837   ±37.67098

Fig. 4.22: Time dependent third harmonic

33

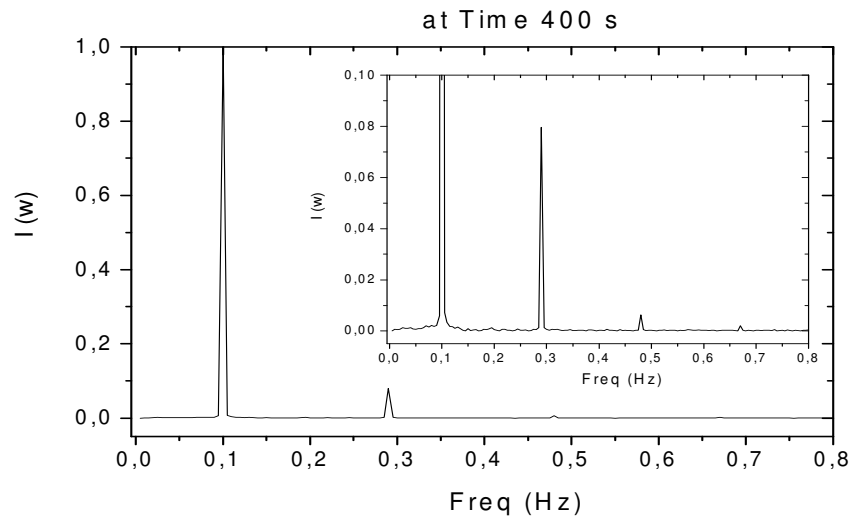The mechanical spectra at a specific time is also shown below.

Fig. 4.23 : A graph showing the first, third and the fifth harmonics

At the end of the orientation process, the sample is cooled, removed, cut into slices and investigated by 2-dimensional small-angle X-ray scattering (2D SAXS) measurements to get X-ray patterns for all three Cartesian directions of the sample. The orientation of the lamellae in the *parallel direction* was obtained using the following conditions as illustrated in Figure 6.8 below: 8 mm parallel plate geometry, gap = 0.9 mm, $\omega_1/2\pi = 0.1$ Hz, $\gamma_0 = 5\%$, $T = 403K$, $t = 10h$.

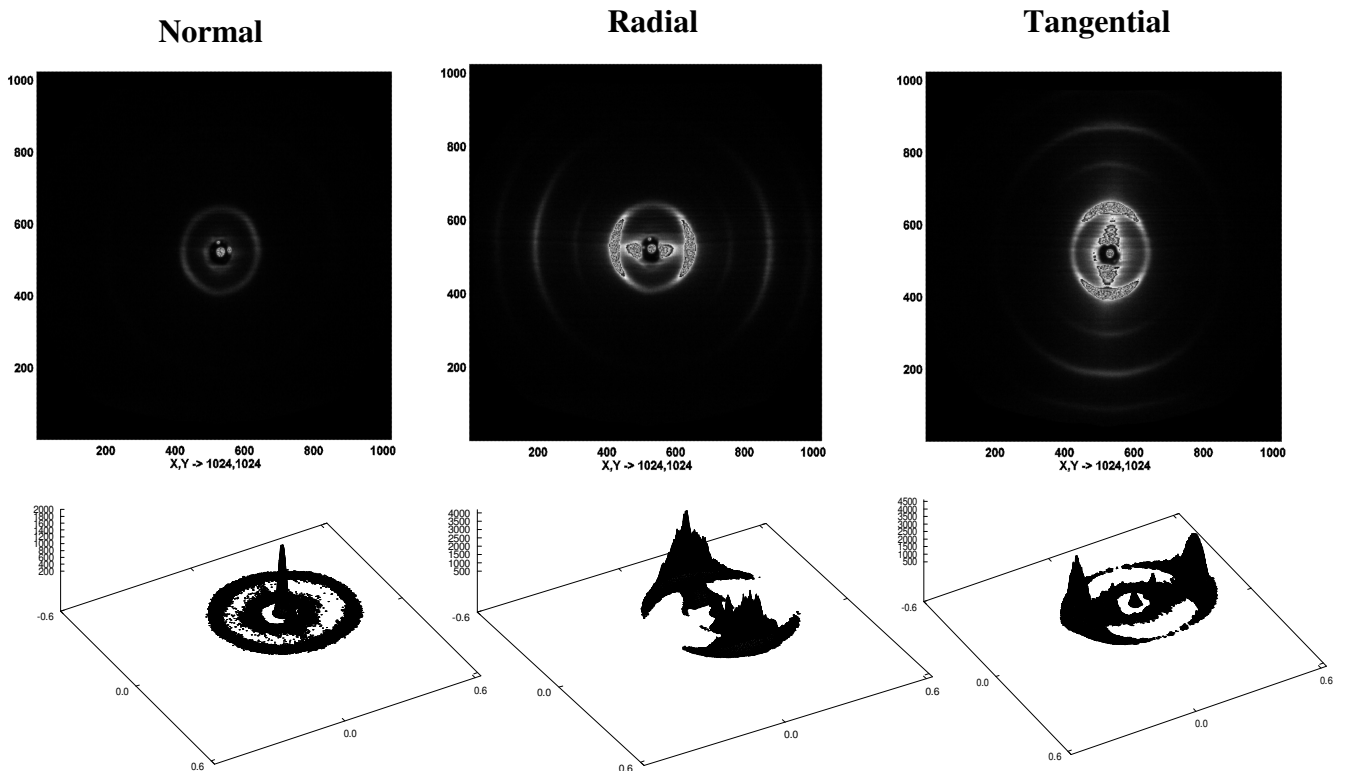**Normal**   **Radial**   **Tangential**

Fig. 4.24: 2-dimensional small-angle X-ray scattering (2D SAXS) measurements

The sample was cut and investigated by 2D WAXS measurements and the following plots obtained.
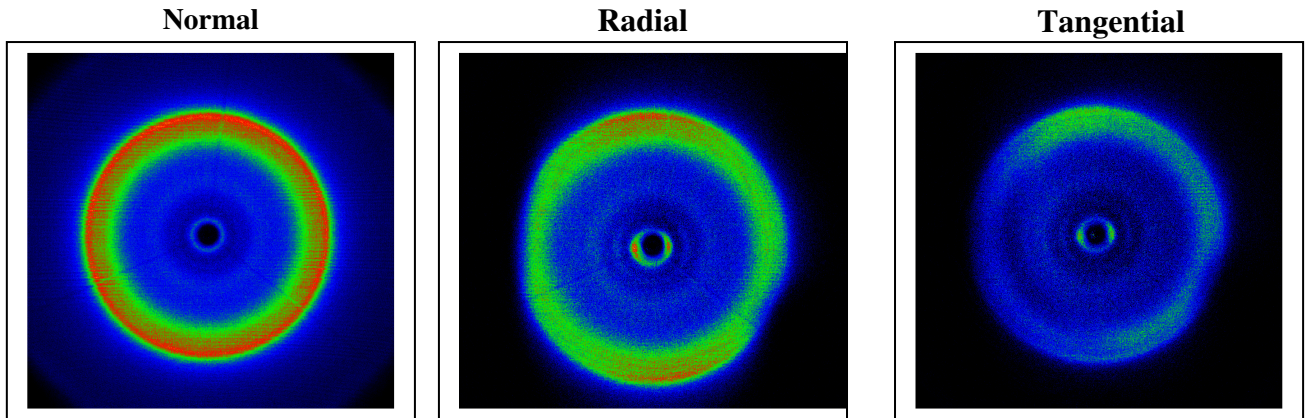
Normal   **Radial**   **Tangential**

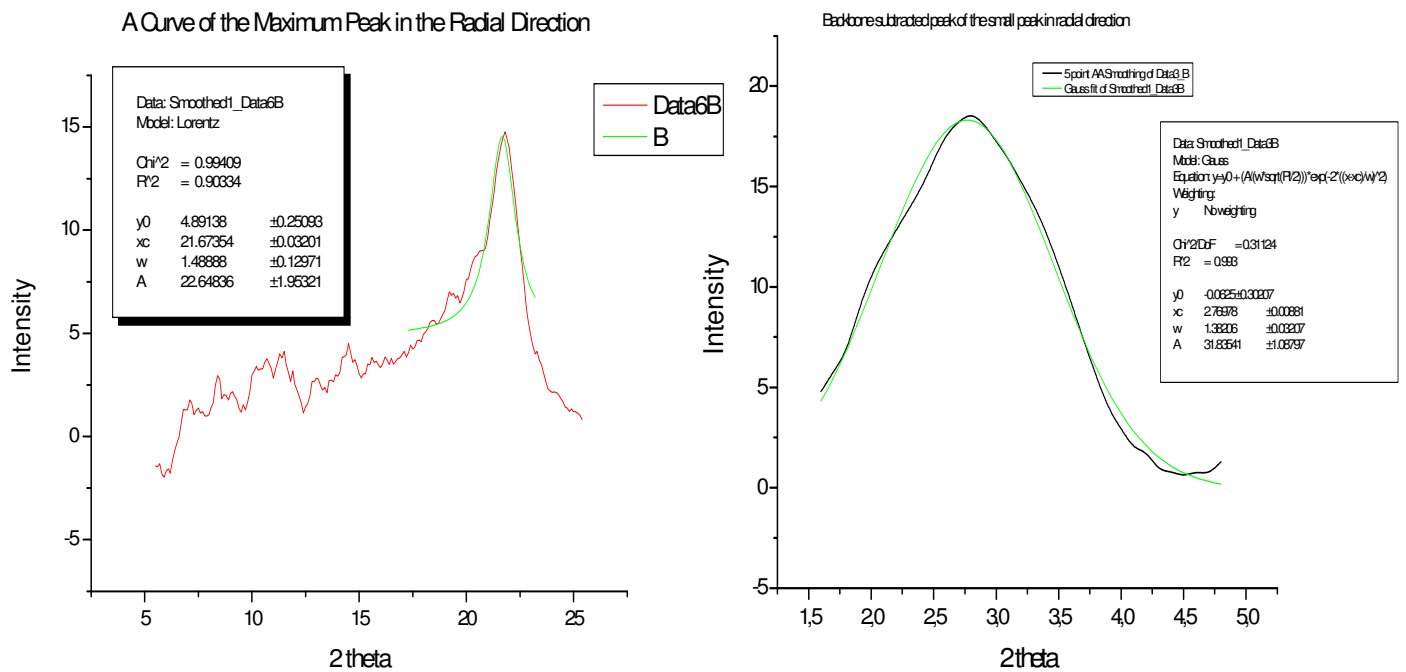Fig. 4.25: 2D WAXS Measurements of the oriented Sample

Plots from the Radial Direction

Fig. 4.26: Integrated Graphs from the Oriented 2D WAXS Graphs in the Radial Direction
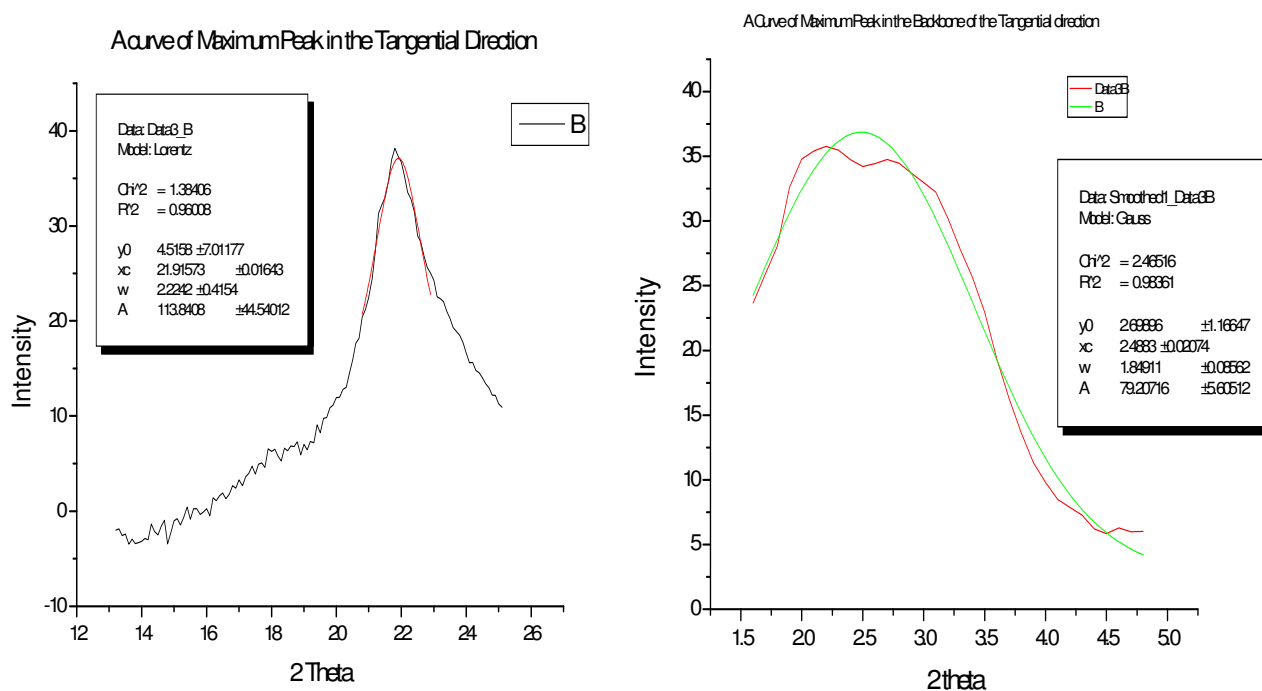
35

Fig. 4.27: Integrated Graphs from the Oriented 2D WAXS Graphs in the Tangential Direction

From the plots of the Radial direction, the sharp peak can be seen around $2\theta = 21.7$ degree corresponding to a bragg's interplaner spacing of ***d ≈ 4.1Å*** . The backbone to backbone peak can also be seen at $2\theta = 2.8$ degrees (***d ≈ 31.6Å***). Again, form the Tangential Radial the sharp peak is also around $2\theta = 21.9$ showing a difference in $2\theta = 0.2$. This indicates that some of the crystalline cylinders within the lamella superstructure shows a more compact interplaner distance. Chapter five gives more explanation in this case.

4.9 Raman Spectroscopy

The sample for the Raman spectra was prepared on quarz substrate from solution of 1.4 Dioxane which was evaporated. FTIR-Raman Spectra were obtained from the Bruker RFS 100 using a laser wavenumber of 15798.3 cm^{-1} at room temperature. In our samples, the measurement was done around the melting temperatures (at room temperature) since there was no chance to cool the sample and also the fear of incorporating ice (water) on the surface of the samples. Hence, the spectrum around the melting temperature was obtained.
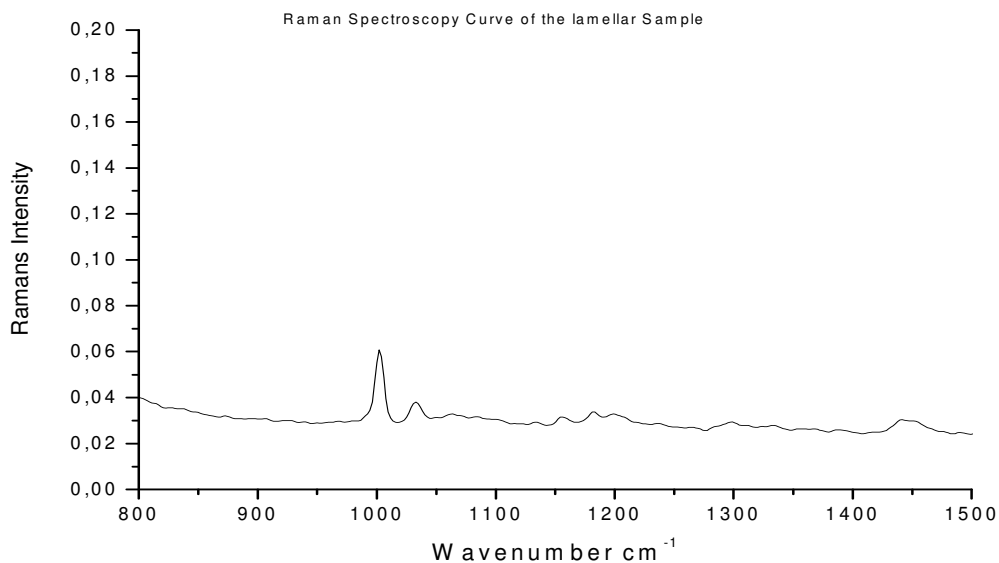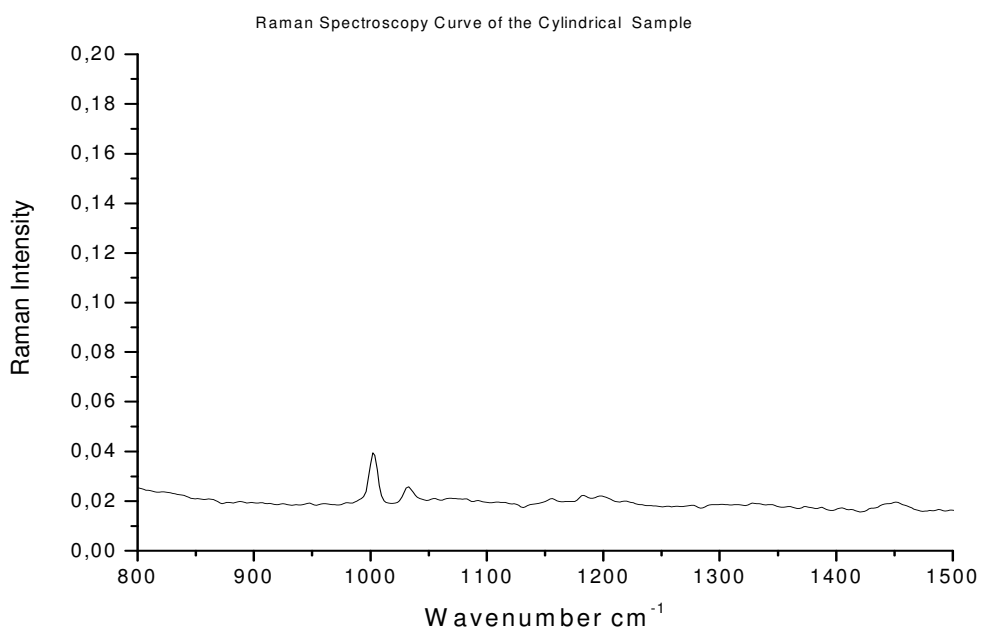
Fig. 4.28: Raman Spectra of lamella sample

Fig. 4.29: Raman Spectra of cylindrical sample

As described earlier on, highly ordered crystalline structures give rise to a characteristic sharp and hence intense Raman spectra than the disordered structures and in C-C chain stretching for hexagonal system, the asymmetric ($\Delta\dot{\upsilon}_{as}$) and symmetric ($\Delta\dot{\upsilon}_{s}$) stretching vibrations occurs at 1063 and 1131 cm^{-1}, respectively. From the spectra above, the peaks are not intense since measurement was done in the molten state of the PODMA. The small sharp peak is near the asymmetric region of 1063cm^{-1} while the other peak can be assigned to stretching of a gauche conformers.

Chapter Five-Discussions

5.1 SAXS

From fig.4.4, the SAXS graph from for the sample 154/25 reveals a typical lamella structure with a q, $2q$, $3q$, $4q$ peaks. The sample 224/12 sample also shows a typical Cylindrical structure with q, $\sqrt{3}\,q$ and $2q$. The intensity of the peaks increases with the increase in the temperature and shifts to the lower angles during melting. There is a formation of an ordered melt of the PODMA in the confined geometry of the amorphous polystyrene. This has been proved from the analysis of the order-disorder transition (ODT), which gave an impression on how constant the SAXS peaks were in the analysis (fig.4.18). Initially, there were only two contrast in electron densities between the semicrystalline PODMA and the amorphous Polystyrene. This produced the two distinct peaks in the SAXS peaks at lower temperatures. After the melting point of the PODMA, the backbone of the PODMA melted completely while some of the crystalline side chain members retained their crystal structures. There was an introduction of a new phase system by the amorphous PODMA melts within the smaller crystallline melts which gave some expansion of the PODMA system and also introduces its own electron density. This behaviour produced the new peak above the melting point of the PODMA as can be seen on the SAXS graphs.

5.2 WAXS

Comparing the WAXS graphs for the combined homopolymer and the block copolymer at room, the PODMA system in the block copolymer can be said to be in a confined geometry of the Polystyrene phase since the backbone to backbone peak cannot be seen.
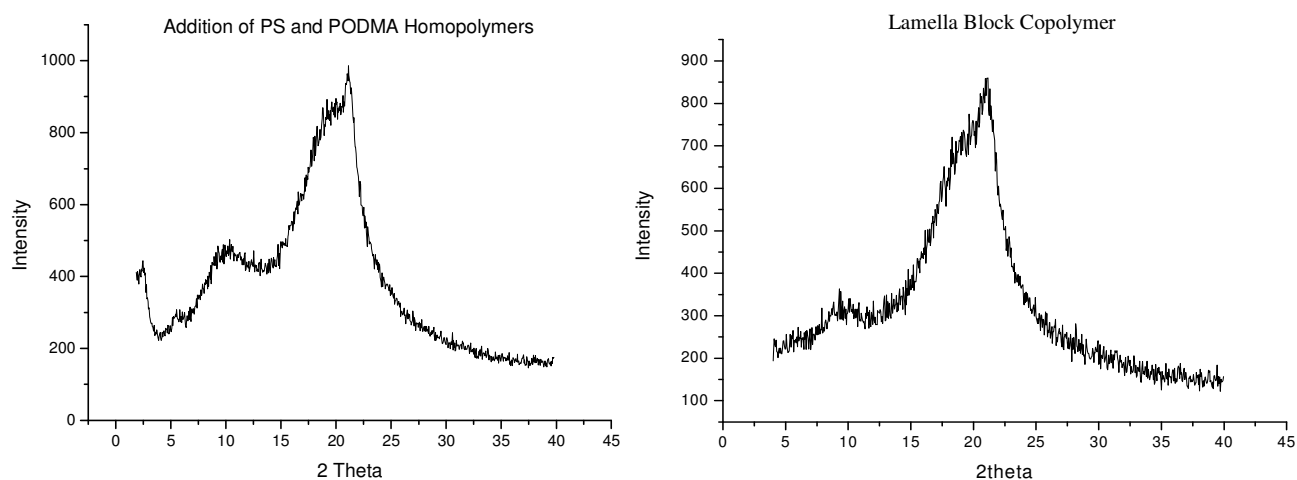

Fig.5.1 Comparisons of combined PS-PODMA and the block copolymer PS-PODMA

In the PODMA homopolymer, the backbone to backbone distance is around $\underline{d_{homo}} \approx 29.4\text{Å}.$ However, after orientation of the blockcopolymer sample, the analysis of the backbone to backbone distance reveals a distance of $\underline{d_b \approx 31.6\text{Å}.}$ The crystalline spacing of the homopolymer is 4.1Å. The middle peak of the PODMA is at $2\theta = 6$ corresponding to a distance of **14.7Å** relating to the extent of the correlation between the crystalline methylene units since the side chain are interconnecting, forming layers[25]. The highest amorphous polystyrene peak can be seen around $2\theta = 19.2$ in the homopolymer but in the block copolymer it was around $2\theta = 19.2$ showing a difference of $2\theta = 0.2$. and the other peak is at $2\theta = 9.8$. Comparing the graph of the PODMA homopolymer at room temperature and the graph of the block copolymer at the same temperature which the PS has been subtracted (figures below), it can be analysed that, crystal hexagonal cylinders are in the same packing at that temperature. At lower temperature (-30^0C) (fig.4.12), the crystal hexagonal cylinders in a more compact form than in the homopolymers ($d_{Homo.} = 4.1$Å and $d_{Blockcop.} = 4.2$ Å).
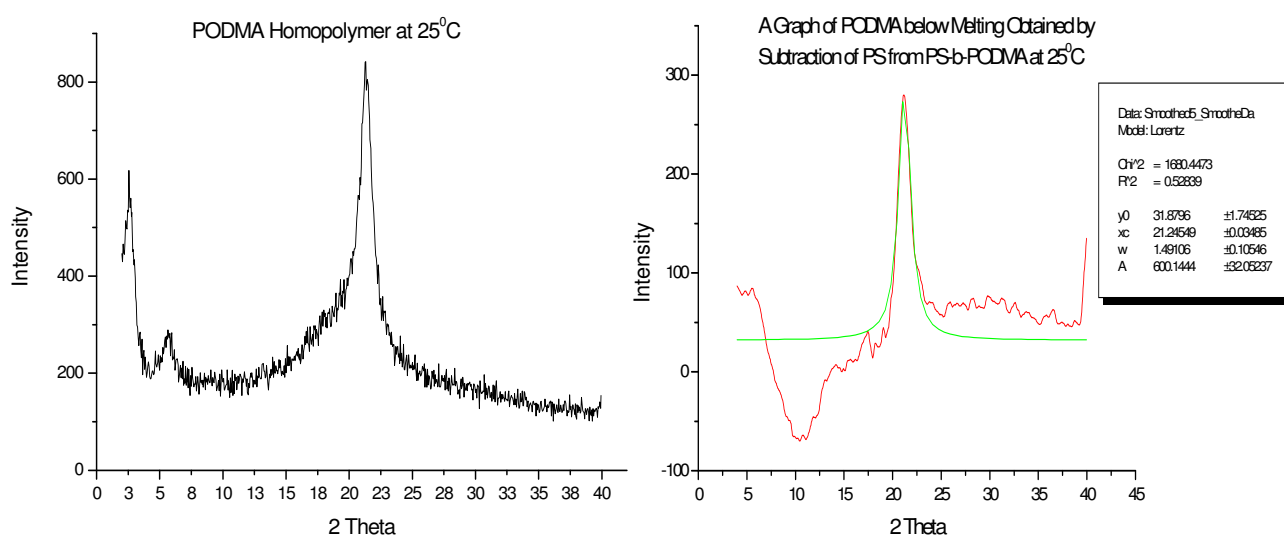

Fig. 5.2 : Comparation of the PODMA homopolymer and PODMA from the Block Copolymer at 25^0C

With this analysis, the side chain crystallization can be said to be arranged perpendicular or slightly inclined to the plane of their backbone in a loose hexagonal modification assumed by many *n*-paraffins a few degrees below their melting point.[48] Amorphous main chains units are connected to 7 to 9 methylene groups which branch atactically from the main chain. These connects the ordered alkane chains, arranged in a hexagonal subcell, separated by 4.2Å.
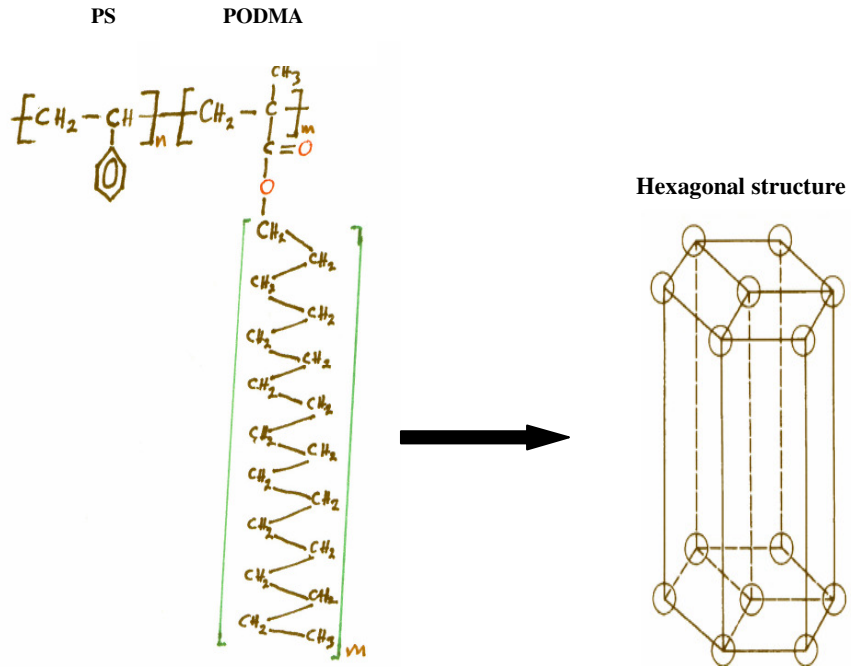
PS   PODMA

Hexagonal structure

Fig.5.3   Crystal structure of the Block copolymer
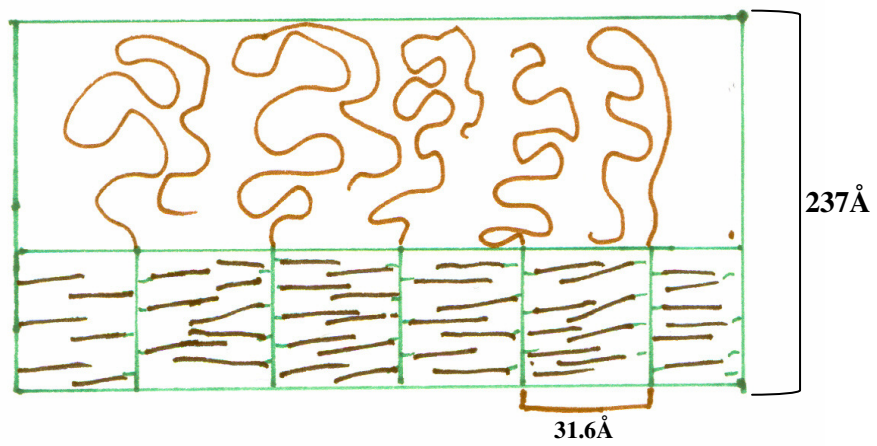

237Å

31.6Å

Fig.5.4   Structural Period of the Block copolymer

5.3 Orientation

From the analysis of the 2D SAXS plots in the three directions of the measurements, it was concluded that a Parallel Orientation has taken place. The model can be seen below. At the Normal position of the X-ray beam, there was no indication of peak which shows that there are no structural periods. At the Radial and tangential direction, there was an oriented peaks revealing that the sample has been parallely oriented as shown in the model below.
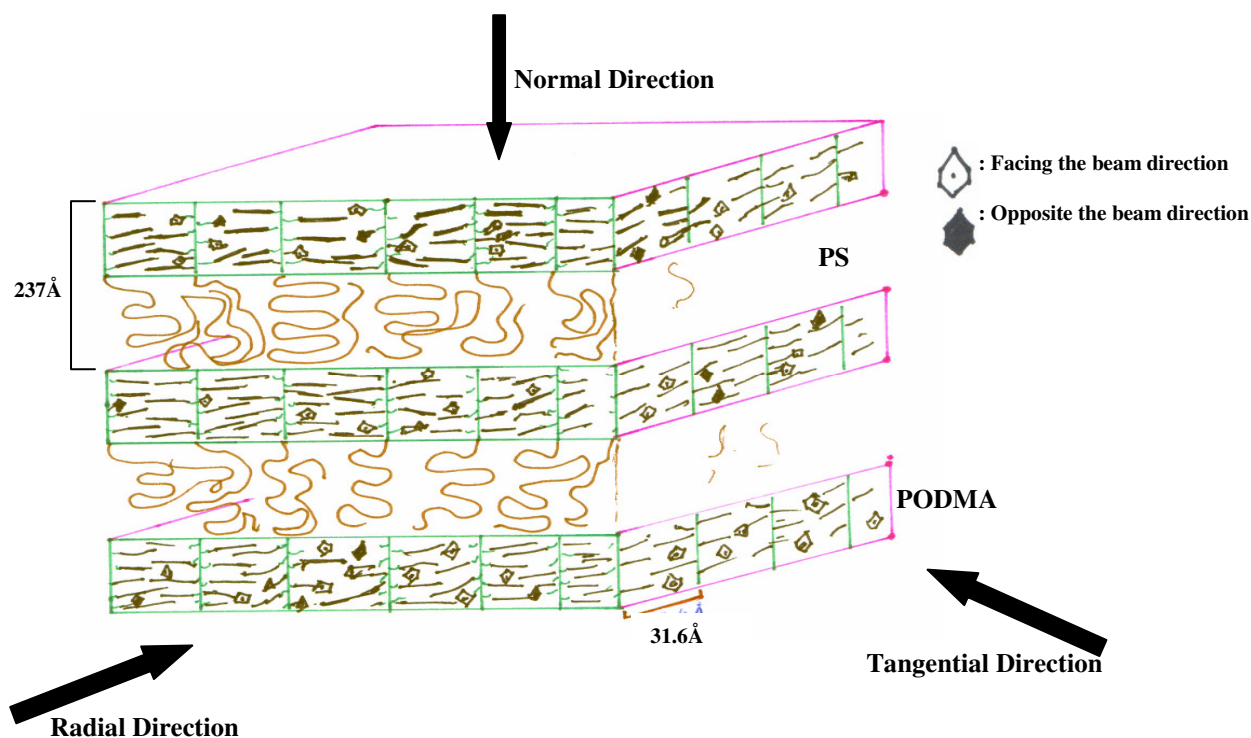

Fig.5.5 Proposed model of the sample

In the analysis of the 2D WAXS data, there was also no indication of any peaks at the normal direction. The intensities 2D WAXS diagram at the normal direction only represents the background of measurements since a supporting medium was used. In the Radial and Tangential direction of the 2D WAXS diagram, there was an indication of a hexagonal peaks. This can be seen after subtraction of the backgrounds in figure 4.26 and 4.27.

The structure can then be said to have the hexagonal side chains crystals parallel to the lamella superstructure and perpendicular to the backbone of the PODMA which is slightly inclined.

5.4 Raman Vibrations

From the Raman spectra of the two samples, it can be concluded that there was an asymmetric ($\Delta\acute{\upsilon}_{as}$) stretching vibrations of the side chains around 1063 cm^{-1}. There was also a gauche stretching near this vibration.

Chapter Six-Conclusion and Recommendation

6.1 Conclusion

The structural behaviour of the Polystyrene-block-PolyOctadecylmethacrylate copolymer system has been clearly underlined. The sample with the PODMA composition, $f_{PODMA} = 0.39$ revealed a lamella structure and the other sample with $f_{PODMA} = 0.18$ also showed a cylindrical structure. The side chain crystallizes with a hexagonally packed cylinders. The hexagonal side chains are perpendicular to the backbone and orients parallel to the lamellar superstructure. Parallel orientation of the lamellar superstructure was obtained. There is asymmetric stretching vibrations of the carbon -carbon in the side chain of the PODMA.

6.2 Recommendation

The analysis has been done on block copolymer system with PODMA having a side chain of 18 carbon members. However, one can vary the number of these side chains carbons to illustrate the crystalline behaviour of the side chains in similar block copolymer system. I also recommend that the isothermal x-ray measurements should be carried out to investigate the crystalline behaviour in the small angle region ($2\theta = 1.5$-2).

References

1. Douzinas K.C., Cohen R.E. ; *Chain Folding in EBEE Semicrystalline Diblock Copolymers*, Macromolcues, 25, 1992, 5030-5035.

2. Kofinas P., Cohen R.E.; Macromolecules ,27, 1994, 3002-3008.

3. Almdal K., Koppi K.A., Bates F.S.; Macromolecules, 25, 1992, 1743.

4. Koppi K.A, Tirell M., Bates F.S.; Phys. Rev. Lett, 70(10), 1993, 1449.

5. Koppi K.A, Tirell M., Bates F.S, Almdal K., Colby R.H; J. Phys. II, 2(11), **1993**, 1941.

6. Zhang FJ, Huang HY, Hu ZJ, Chen YZ, He TB *Crystallization of Weakly Segregated Poly(styrene-b-epsilon-caprolactone) diblock copolymer in thin films*, Langmuir, (2003) 19 iss: 24, p 10100.

7. Imaizumi K., Ono T., Natori, Shinichi S, Takeda K. Article on *Microphase-separated structure of 1,3-Cyclohexadiene/Butadiene Triblock Copolymers and Its Effect on Mechanical and Thermal Properties*, October, 2000.

8. Hamley I. W., *The Physcis of Block Copolymers*, (1998),2-6.

9. Flory P.J., *Principles of Polymer Chemistry*, Cornell University Press, Ithaca, 1953.

10. Jun-Ting Xu, Jian-Jun Yuan,Si-Yuan Cheng, *SAXS/WAXS/DSC studies on crystallization of a polystyrene-b-poly(ethylene oxide)-b-polystyrene triblock copolymer with lamellar morphology and low glass transition temperature*, European Polymer Journal, 39, Iss. 11. (2003) Pp. 2091-2098.

11. Hamley I.W., Fairclough J.P.A., Bates F.S., Ryan A.J., Polymer, **39,** (1997), 1429.

12. Avrami M., *Journal of Chemical Physics*, **7**, (1939),1103.

13. Gedde U.W., *Polymer Physics*, Chapman and hall, London, 1995.

14. Hamley I. W., *The Physcis of Block Copolymers*, (1998),314-323.

15. Almdal K., Koppi K.A., Bates F.S.; Multiple Ordered Phases in a Block Copolymer melt, Macromolecules, 25, 1992, 1743-1751.

16. Kofinas P., Cohen R.E., *Macromolecules*, **27**, (1994),3002.

17. Alexander L.E.; X-Ray Diffraction methods in Polymer Science, 1979, pp.33-63.

18. Kausche, *Wide Angle X-rays Scattering, Lab Notes*, Halle (saale), 2003.

19. Oelschlaeger C., Wilhem M., Gutmann J; Microphase Orientation and Re-orientation in Block Copolymer Melt as Detected Via a FT –Rheology; Presentation, MPIP, Mainz

20. Neidhoefer T.; Fourier-Transform Rheology on Anionically Synthesised Polymer Melts and Solutions of various Topology, Doctorial Thesis, MPIP, Mainz, 2003.

21. Langela M., Wiesner U., Spiess H. W., Wilhelm M.: *Microphase Reorientation in Block Copolymer Melts As Detected via FT Rheology and 2D SAXS, Macromolecules*, **35** (8), 3198-3204, 2002.

22. Anderson   L. G., CU-Denver Chemistry Department homepage, University of Colorado, (2000).

23. Hendra P., Jones C., Warnes G.; Fourier Transform Raman Spectroscopy; Inst. And Chem. Appl., 1991.

24. lee K., Wegner G.: *Vibrational spectroscopic studies of linear and cyclic alkanes*, *Polymer*, 889, (28), 1987.

25. Mierzwa M., Floudas G., Stepanek P., Wegner G.: *Physical Review B*, (**62**) No. 21 14012-14019, 2000.

26. Wunderlich B.,*Macomolecular Physics*, Vol **3**, 317, New York, 1980.

27. Whitmore M.D, Noolandi J., *Macromolecules*, **21** , (1988), 1482.

28. Beiner M., *Relaxation in Poly(alkyl methacrylate)s: Crossover Region and Nano-Separation*: *Macromol. Rapid Commun*, 22, (2001),869.

29. Hempel E., Beiner M., Huth H., *Thermochim. Acta* 403 (2003) 105-114.

30. Balta-Calleja F.J., Vonk C.G., X-ray Scattering of Synthetic Polymers, Elsevier, London, 1989.